A New Method to Simulate Extreme-Mass-Ratio Inspirals for the Laser Interferometer Space Antenna

Priscilla Cañizares Martínez

Director: Dr. Carlos Fernández Sopuerta

Treball de recerca *presentat al* ***Departament de Física*** *de la* ***Universitat Autònoma de Barcelona*** *per Priscilla Cañizares Martínez, com a Treball de Recerca Tutelat sota la direccio del Dr. Carlos Fernández Sopuerta.*

Bellaterra, Març de 2009

Carlos Fernández Sopuerta, Investigador de l'*Institut de Ciències de l'Espai (CSIC-IEEC)*, CERTIFICA: Que la present memória, que porta per títol "A New Method to Simulate Extreme-Mass-Ratio Inspirals for the Laser Interferometer Space Antenna", ha sigut realitzada sota la seva direcció per Priscilla Cañizares Martínez i constitueix el seu Treball de Recerca Tutelat del Programa de Doctorat en Física de la Universitat Autònoma de Barcelona.

Bellaterra, Març de 2009

Carlos Fernández Sopuerta.

Contents

Chapter 1

Introduction

Gravitational Waves (GWs) are ripples in the curvature of the spacetime, generated by accelerated masses and energy of any kind, which travel at the speed of light. The potentially detectable GWs are emitted by the bulk motion of their sources and not by their basic components (atoms, molecules, etc.), like in the case of electromagnetic waves. As the mechanism which lead to the generation of gravitational and electromagnetic waves is different, so is the kind of information that they carry and also their detection methods. The most attractive feature of GWs is that they are not attenuated or scattered significantly on their way through the spacetime. Hence, they offer us information which could not be obtained by other means like the direct observation of black holes or information of just a fraction of second after the Big Bang.

The existence of GWs is the last prediction of General Relativity to be verified in a direct way, although we have strong indirect evidence of their existence: the measured rate of change of the orbital period of the binary pulsar PSR1913+16 [Hulse & Taylor (1975)], which agrees with that expected from the emission of gravitational waves in general relativity to within about 0.2% [Weisberg & Taylor (2005)].

The aim of the emergent branch of *Gravitational Wave Astronomy* is let us access to a new kind of information about astrophysical systems and the universe itself by means of the direct detection of GWs. In this regard, laser interferometers sufficiently sensitive to measure the small changes ($\Delta L/L \sim 10^{-22} - 10^{-23}$) produced by the passage of a GW have been developed. By one hand, there are the ground-based detectors, which will be sensitive to frequencies in the range $10^{-1} - 10^{3}$Hz (high frequency range), as the Laser Interferometer Gravitational-Wave Observatory[1] (LIGO) and the Italian and French detector VIRGO[2]. This first generation of ground-based interferometric detectors has a real chance of detecting the GWs for the first time ever. Nevertheless, the rate of detected events expected, on the basis of the astrophysical population models, will be low. Thus, such detectors are being upgraded (Advanced LIGO/VIRGO) in order to improve their sensitivity. On the other hand, there is a planned space-based detector, the Laser Interferometer Space Antenna (LISA)[3], an ESA-NASA mission, which aims to detect gravitational waves in the low frequency range, $10^{-4} - 1$ Hz.

In this work we are going to study a model of the most promising sources of GWs for LISA. These are the systems made up of an stellar compact object (SCO), $m = 1 - 50M_{\odot}$, inspiralling into a massive black hole (MBH), $M = 10^{4} - 10^{7}M_{\odot}$. These systems are called

[1] http://www.ligo.caltech.edu/advLIGO

[2] http://wwwcascina.virgo.infn.it/advirgo

[3] http://www.esa.int, http://lisa.jpl.nasa.gov

Extreme Mass-Ratio Inspirals (EMRIs) due to the mass ratios involved are in the range $\mu = m/M \sim 10^{-7} - 10^{-3}$.
During the last year before plunge into the MBH, [Finn & Thorne (2000)] an EMRI will spend about 10^5 cycles orbiting inside the LISA band. However, the gravitational-wave signals from EMRIs will be buried in the LISA data stream with the instrumental noise and the gravitational wave foreground mostly from galactic binaries. This translates in a need for accurate theoretical templates in order to compare them with the detected signals and extract the parameters containing the relevant physical information separating, in this way, the signal from the noise. This separation will be carried out by cross-correlating the detected LISA data with the theoretical waveforms (match filtering technique).
Modeling EMRIs is a two body problem which could be easy to solve if we were in Newtonian gravity, but in general relativity, due to the complexity of solving the Einstein field equations, its a more challenging problem. One of the main reasons is that in the general relativistic problem the SCO orbit shrinks due to the emission of energy and angular momentum in GWs, until plunging into the MBH. This inspiral decay is a *gravitational backreaction* or *radiation reaction* effect. In this way, a correct treatment has to incorporate the radiation reaction effects in the motion of the SCO; that is, we have to compute the gravitational perturbations introduced by the SCO in the gravitational field of the MBH, and how these perturbations affect the SCO motion. In order to do so, we can use perturbative methods due to the extreme-mass ratio involved in the problem, where the backreaction is described as a local *self-force* which, in turn, can be computed in terms of the perturbations generated by the SCO on the MBH background.
In order to solve the perturbative equations for the EMRI problem, we need to use numerical methods, either in the frequency- or in the time-domain. Here, we present a new computational method with the aim of computing the self-force. Calculations in the time-domain turn out to be more convenient to deal with eccentric orbits, which are the ones of interest for LISA. Usually, in time-domain methods one is bounded to resolve simultaneously very different length scales and time scales associated with the particle and the black hole. We will see that our method avoids the small scales associated with the particle and hence, we only have to care about resolving the field.
The organization of the present work is as follows: in chapter 2 we introduce the basics of the generation and detection of GWs in the weak field regime, the one of interest for GW detection. We also introduce to the science of LISA and the self-force problem. Later, in chapter 3, we give an introduction to the Pseudospectral Collocation Method, used to solve the equations of our problem, with a brief review of Chebyshev polynomials and the spectral filter used in our numerical code. In chapter 4 we present the problem that we study in this work: a charged scalar particle orbiting a non-rotating black hole. We also include the basic formulae for the computation of the self-force via the mode-sum regularization scheme. In this chapter, we also introduce the mathematical developments necessary to apply the pseudospectral methods to our problem and the evolution algorithm used. In chapter 5, we test our numerical code and give the results of computations of the self-force for several circular orbits, including the innermost stable circular orbit ($r = 6M$). In chapter 6 we draw conclusions from the results shown and discuss possible future avenues in the development of these techniques for the simulations of EMRIs. Throughout this work we use the metric signature $(-,+,+,+)$ and geometric units, in which $G = c = 1$.

Chapter 2

Basics of Gravitational-Wave Physics: Generation, Detection and Modeling

The Einstein field equations relate the stress-energy of matter with the spacetime geometry. In an arbitrary coordinate system the Einstein field equations are given by [Weinberg (1972)]

$$G_{\mu\nu} = 8\pi T_{\mu\nu} \ , \tag{2.1}$$

where $G_{\mu\nu}$ are the components of the Einstein tensor and $T_{\mu\nu}$ are the components of stress-energy tensor. $G_{\mu\nu}$ is related with the geometry of spacetime through the Riemann curvature tensor $R_{\alpha\mu\beta\nu}$, which is zero for a flat spacetime, by

$$G_{\mu\nu} = R_{\mu\nu} - \frac{1}{2} g_{\mu\nu} R \ , \tag{2.2}$$

where $g_{\mu\nu}$ are the spacetime metric components, $R_{\mu\nu} = R^{\alpha}{}_{\mu\alpha\nu}$ are the Ricci tensor components, and $R = g^{\mu\nu} R_{\mu\nu}$ is the Ricci scalar. In this way, equations (2.1) and (2.2) show how the stress-energy of matter generates curvature which is the manifestation of gravity.

As we have mentioned above, gravitational waves are ripples in the curvature of spacetime and thus, due to the no-liniality of (2.1), their propagation is affected by themselves. This nonlinearity is the responsible that we are not able to find general radiative solutions of the exact Einstein field equations.

Since the gravitational waves that will be detected will have very low intensity far away from the source, at the observer location, they can be described by the *weak field approximation*. In this approximation they do not carry enough energy and angular momentum to affect their own propagation and the equations to describe them can be linearized.

In the weak field approximation we consider a region of the spacetime bigger than the characteristic wavelength of the GW, λ, but smaller than the background curvature. In such a region we can introduce a Minkowski background $\eta_{\mu\nu}$. Thus, when a GW passes through this locally flat region it will produce a little perturbation of the background flatness, $h_{\mu\nu}$, which changes the spacetime metric:

$$g_{\mu\nu} = \eta_{\mu\nu} + h_{\mu\nu}, \tag{2.3}$$

where $|h_{\mu\nu}| \ll |\eta_{\mu\nu}|$.

In the Lorentz gauge

$$\partial_{\mu}(h^{\mu\nu} - 1/2\eta^{\mu\nu}h) = 0, \tag{2.4}$$

the linearized Einstein field equations [Weinberg (1972)] are

$$\partial_{\mu}\partial^{\mu}h_{\mu\nu} = -16\pi S_{\mu\nu}, \tag{2.5}$$

where $S_{\mu\nu} = T_{\mu\nu} - \frac{1}{2}\eta_{\mu\nu}T^{\mu}_{\nu}$.
One solution of equation (2.5) is the retarded potential which, in terms of the Fourier components of the energy-momentum tensor, can by expressed as

$$h_{\mu\nu}(\mathbf{x},t) = 4\int_0^\infty d\omega \int d^3\mathbf{x}' \frac{S_{\mu\nu}(\mathbf{x}',\omega)\exp\{-i\omega t + i\omega|\mathbf{x}-\mathbf{x}'|\} + c.c.}{|\mathbf{x}-\mathbf{x}'|}, \tag{2.6}$$

where *c.c.* denotes the complex conjugate.
Far from their source, GWs will have fronts with radii of curvature large compared to λ [Wald (1984)] then, each single frequency component of $h_{\mu\nu}$ looks like a plane wave

$$h_{\mu\nu}(\mathbf{x},t) = \varepsilon_{\mu\nu}(\mathbf{x},\omega)e^{ik_\mu x^\mu} + c.c. \tag{2.7}$$

where the wavelike vector k^μ ($k^\mu k_\mu = 0$) is given by $\mathbf{k} \equiv \omega\hat{n}$, where $\hat{n} = (\hat{x},\hat{y},\hat{z})$, and $k^0 \equiv \omega$, and the polarization tensor $\varepsilon_{\mu\nu}$ is:

$$\varepsilon_{\mu\nu} \equiv \frac{4}{r}\int d^3\mathbf{x}' S_{\mu\nu}(\mathbf{x}',\omega)e^{-i\mathbf{k}\cdot\mathbf{x}'} \ , \tag{2.8}$$

which fulfills the conditions: $k_\mu\varepsilon^\mu{}_\nu = 0$ and $\varepsilon^\nu{}_\nu = 0$. These conditions imply that at most five components are independent. These five components reduce to two components if we use the gauge freedom left. A convenient gauge is the *transverse, traceless gauge* (TT), (ε_{12} and $\varepsilon_{11} = -\varepsilon_{22}$), where the metric perturbation components fulfill

$$h_{\mu 0} = 0, \qquad h_{jj} = 0, \qquad \partial_j h_{ij} = 0, \quad \text{where} \quad i = 1,2,3 \ , \tag{2.9}$$

and $h_{ii} := \sum_{i=1}^{3} h_{ii}$. Thus, the non-vanishing components of the metric perturbation are the h_{ij}, where only two of them are independent, leaving six wave equations which for vacuum ($T_{\mu\nu} = 0$) spacetime are given by

$$\partial^\mu\partial_\mu h_{ij} = 0. \tag{2.10}$$

Without loss of generality we assume that the GW propagates along the z-direction, thus the non-vanishing components of h_{ij} are

$$h_+ \ := \ h^{TT}_{xx} = -h^{TT}_{yy}, \tag{2.11}$$

$$h_\times \ := \ h^{TT}_{xy} = h^{TT}_{yx} \ , \tag{2.12}$$

which coincide with two independent polarization states of the GW. Therefore, a GW is described. Thus, a general GW can be described as a combination of these two polarizations, h_+ and $h_\times$:

$$h^{TT}_{ij} \equiv \begin{pmatrix} h_+ & h_\times & 0 \\ h_\times & h_+ & 0 \\ 0 & 0 & 0 \end{pmatrix} \cos[\omega(t-z)] \ , \tag{2.13}$$

In order to detect GWs, we need to know how they interact with matter. To that end, suppose we have two non-spinning nearby free falling test particles which are moving along geodesics $x^\mu(\tau)$ and $x^\mu(\tau) + \delta x^\mu(\tau)$, with $\delta x^\mu(\tau)$ smaller than the scale on which the gravitational field varies. These particles will have a relative motion due to the presence of the gravitational field of the GW, which can be evaluated using the equation for the geodesic deviation [Weinberg (1972)]

$$\nabla_u\nabla_u\delta x^\mu = -R^\mu{}_{\nu\lambda\rho}\frac{dx^\nu}{d\tau}\delta x^\lambda\frac{dx^\rho}{d\tau}, \tag{2.14}$$

where ∇_u denotes the covariant derivative along the curve $x^\mu(\tau)$, $\nabla_u = \frac{dx^\mu}{dt}\nabla_\mu$, and $R_{\mu\nu\lambda\rho}$ is the Riemann-Christoffel curvature tensor, which at linear order in $h_{\mu\nu}$, reads

$$R_{\mu\nu\lambda\rho} = \frac{1}{2}(\partial_{\lambda\nu}h_{\mu\rho} + \partial_{\rho\mu}h_{\nu\lambda} - \partial_{\lambda\mu}h_{\nu\rho} - \partial_{\rho\nu}h_{\mu\lambda}), \tag{2.15}$$

Then, the tidal gravitational force (2.14), in the TT gauge (2.9), can be expressed as

$$R_{i0j0} = \frac{-1}{2}h^{TT}_{ij,00}. \tag{2.16}$$

On a local inertial coordinate system along a geodesic ($t = \tau$), equation (2.14) is given by

$$\frac{d^2\delta x_j}{dt^2} = \frac{1}{2}\frac{\partial^2 h^{TT}_{ij,00}}{\partial t^2}\delta x^i. \tag{2.17}$$

Before the wave arrives, $h_{ij} = 0$ and $\delta x_j = 0$, the test particles are set at relative rest to one another at a distance $x^i(0)x_i(0) = L^2$, where x^i is the vector that joins the two test particles. Then, by integrating equation (2.17) we obtain

$$\delta x_j = \frac{1}{2}h^{TT}_{ji}x^i_0. \tag{2.18}$$

In other words, the dimensionless gravitational strain is $h = \delta L/L$, where $\delta L \equiv \delta x$.
We now replace the test particles by the mirrors of an interferometer of arm lengths $L_1 = L_2 = L$. Then, when a gravitational wave passes through it pushes the mirrors back and forth relative to each other changing the arm length difference, $\delta L(t) = L_1 - L_2$. If we make the axis of the wave polarization coincide with the arm directions then [Thorne (1997)]

$$\frac{\delta L(t)}{L} = C_+h_+(t) + C_\times h_\times(t) \equiv h(t), \tag{2.19}$$

where the coefficients C_+ and $C_\times$ depend on the orientation of the source and the detector ($h_\times$ and h_+ are given in equation (2.12)) and $h(t)$ is the called gravitational wave strain as it describes the detector response. The time evolution of $h(t)$ gives us a measurement of the waveform of the GWs detected. This is the principle on which relies interferometric gravitational wave detectors as LISA or LIGO.

2.1 LISA: The Laser Interferometer Space Antenna

The detection and study of the gravitational radiation coming from astrophysical and cosmological sources is the purpose of the new emergent area of *Gravitational Wave Astronomy*.
In this regard, there is the ESA/NASA collaborative space mission LISA, planned to be launched in the next decade, which aims to detect gravitational waves in the low frequency range, $10^{-4} - 1$ Hz, see figure 2.1. This band is not accessible by ground-based gravitational wave detectors due to gravity gradient noise and the physical constraints imposed by their arm-lengths, as LIGO or VIRGO, whose frequency range lies around $10^{-1} - 10^3$Hz (high frequency range). Ground-based detectors are being improved to a more sensitive generation of detectors called Advanced LIGO and Advanced VIRGO, see figure 2.1.

LISA will be composed of three spacecrafts set in an equilateral triangle configuration, to form two independent Michelson interferometer, (see figure 2.2). Its center will orbit around the Sun, following the Earth at a distance of about 50×10^6 km, at 20^o behind in the ecliptic

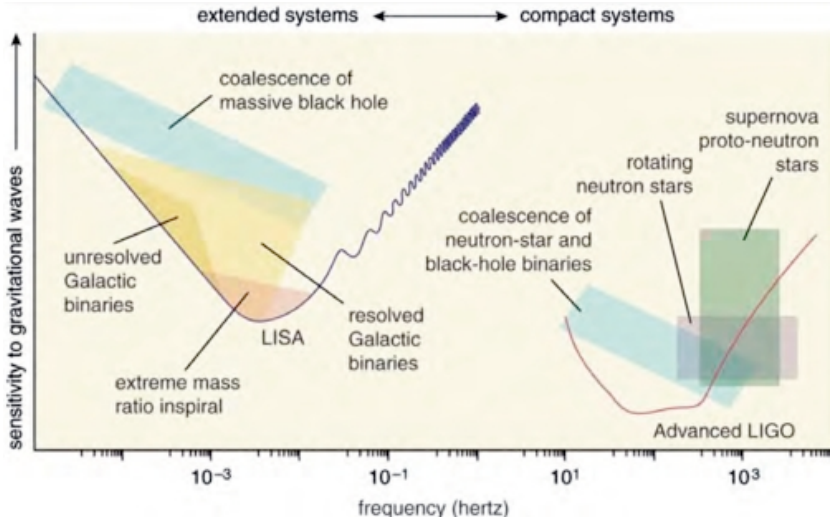

Figure 2.1: In this figure we show the gravitational wave sensitivities for LISA and Advanced LIGO. We can see how these two detectors are complementary due that they will detect different astrophysical systems/frequencies

(to minimize the effects of the Earth's gravity), and will lie in a plane tilted at 60º, (see figure 2.2). The distance between spacecrafts, 5×10^6 km, will be modified mainly by GWs passing through through of GWs. The unperturbed triangular configuration of LISA will be almost rigid, since it will depend on the orbit of each spacecraft and the triangular shape will twist and rotate around its center with a period of a year. Inside each spacecraft, two proof masses will be kept on geodesic orbit by a drag-free system. This system compensates, through the use of micro-thrusters, for the external forces acting on the spacecraft by keeping it at its proper position with respect to the proof mass.

LISA will detect mainly GWs from MBH mergers, EMRIs, Galactic binaries, cosmic strings

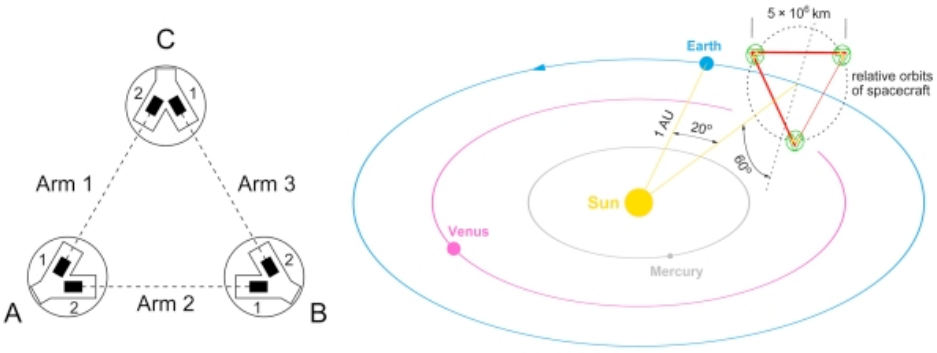

Figure 2.2: In this figure is show the configuration of the LISA spacecrafts (left) and the position of LISA in its orbit around the Sun (right).

and phase transitions. The main scientific goals expected to be achieved by the detection of GWs from these sources are[1] :

- Massive black hole mergers: With the GWs coming from these sources we can figure out how massive black holes form, grow, and interact over the entire history of galaxy formation and learn about galaxy formation itself; we can also follow the inspiral and

[1] http://sci.esa.int/science-e/www/object/index.cfm?fobjectid=41272♯

merger of massive binary black holes and measure the small black hole parameters. With these information we can test general relativity and the Kerr solution describing spinning black holes. Finally, we can perform precise measurements of gravitational-absolute luminosity distances to high redshift, up to $z \simeq 20$, in order to obtain measurements of the Hubble constant and information about dark energy.

- Extreme-mass-ratio inspirals: They are one of the main sources of GWs for LISA. They are binary systems composed of one stellar mass compact object (SCO) $m = 1 - 50 M_{\odot}$, (a white dwarf, a neutron star, or a stellar-mass black hole) inspiralling into a massive black hole (MBH), $M = 10^4 - 10^7 M_{\odot}$. These systems are referred to as EMRIs due that the mass ratios involved are in the range $\mu = m/M \sim 10^{-7} - 10^{-3}$. With the EMRIs GWs, LISA will map isolated massive black holes with high precision. Hence, we will be able to verify whether black holes are described by the Kerr metric and the "no-hair" conjecture to very high precision. We can also obtain census of compact objects near galactic centers. There is also the possibility of testing galaxy formation models and measure cosmological parameters.

- Galactic binaries: With these sources of GWs LISA will be able to study thousands of compact binary stars in the Galaxy in order to get more information about stellar evolution. We can also obtain information about populations of compact objects through the galaxy.

- Cosmic strings and phase transitions: This kind of GWs sources will let LISA find new phenomena of nature which are undetected by using light or other particles. For example, LISA may be able to measure phase transitions of new forces of nature or extra dimensions of space which may have caused explosive bubble growth and efficient gravitational wave production.

2.2 The Extreme Mass-Ratio Inspiral (EMRI) Problem

As we have mentioned in the introduction, EMRI systems, the capture of SCO by a MBH, located at the galactic center, have been identified as one of the promising sources of GWs for the space-based interferometric detector LISA. Sometimes, the SCO falls into the MBH gravitational field and is set at a close orbit around it. Then, the orbit of the SCO shrinks by the emission of energy and angular momentum in the form of GWs, whereas it performs an inspiral which ends up with the SCO plunging into the MBH (see Sec. 2.1). These systems involve highly eccentric, nonequatorial, and relativistic orbits around rapidly rotating black holes.
LISA will be able to detect $10 - 10^3$ EMRI/yr, [Gair et al. (2004)], [Hopman & Alexander (2006)], up to distances within $1\,Gpc$, [Sigurdsson & Rees (1996)]. Recently, it has been suggested, [Brown et al. (2007)], [Mandel et al. (2007)], that inspirals of SCOs into intermediate-mass black holes (IMBHs), with masses in the range $50 - 350\,M_{\odot}$ and presumably located in globular clusters, could be detected by future second-generation ground interferometers like Advanced LIGO and Advanced VIRGO.
During the inspiral, an EMRI will spend many cycles inside the LISA band, of the order of $\sim 10^5$ during the last year before plunge into the MBH, [Finn & Thorne (2000)]. In this way the SCO will track much of the geometry of the massive black hole spacetime, which will be encoded in the structure of the gravitational waves emitted. However, the gravitational-wave signals from EMRIs will be buried in the LISA data stream with the instrumental noise and

the gravitational wave foreground (produced by compact binaries in the LISA band). Hence, there is a need for accurate theoretical templates to compare the detected signals and extract the parameters containing the relevant physical information. The obtention of the physical information from the collected data will depend on data-analysis strategies, these data analysis techniques, like the match filter, require a very detailed and accurate modeling of the source. This modeling involves solving the equations of motion for the SCO in the field of the rotating MBH, to develop methods to extract from the trajectories the gravitational wave signals [Poisson (2005)].

Due to the extreme mass ratio, we can model EMRIs using *black hole perturbation theory*. In this approach the perturbative equations take into account all the general relativistic effects of the background spacetime and they are applicable to arbitrary orbits of the SCO. Furthermore, with the help of numerical techniques, the gravitational waves from highly relativistic orbits can be calculated.

In black hole perturbation theory, the perturbations around the black hole spacetime are evaluated to linear order in the mass ratio μ. Moreover, for non-rotating black holes a single master equation for the odd parity part [Regge & Wheeler (1957)] and another one for the even parity part of the metric perturbations [Zerilli (1970)] can be derived. In this way, the equations are decoupled of the rest of the metric perturbations and hence, the problem has been simplified enormously. Solving these equations one can describe EMRIs in the *adiabatic* approximation [Mino (2003); Pound et al. (2005); Pound & Poisson (2008); Mino (2008); Hinderer & Flanagan (2008)], by assuming that the orbital decay is exclusively due to dissipative effects of the perturbations. Then, we are neglecting conservative effects that may come important when we need to obtain many cycles of the EMRI waveforms. To account for these effects we can follow the self-force scheme [Poisson (2005); Mino et al. (1997); Quinn & Wald (1997)]. In this scheme the gravitational backreaction is described in terms of a *local* force, the self-force, acting on the SCO. To compute the self-force one needs a scheme to regularize the metric perturbations at the SCO location (they are infinite since the SCO is usually described as a point like object). Thus is similar to what happens in electrodynamics with accelerated charged particles [Barut (1980); Jackson (1999)]. However, such a regularization scheme is not available for the Regge-Wheeler gauge an one has to work in a different gauge. A convenient gauge is the harmonic gauge [Barack & Ori (2000); Barack (2000, 2001); Mino et al. (2003); Barack et al. (2002); Barack & Ori (2002); Detweiler et al. (2003); Haas & Poisson (2006)].

In this work we propose a new scheme and a new numerical technique for computing the SCO perturbations and the self-force. As the partial differential equations (PDEs) associated with the perturbative EMRI problem are very difficult to solve completely analytically, we need to resort to numerical methods based on either frequency-domain or time-domain techniques. The frequency-domain approach provides accurate results for EMRIs with moderate eccentricities [Davis et al. (1972); Detweiler (1978); Detweiler & Szedenits (1979); Cutler et al. (1994); Poisson (1995, 1997)], but has more difficulties dealing with highly eccentric orbits, which are of interest for LISA, since one has to sum over a large number of modes to obtain a good accuracy and the convergence is very slow. On the other hand, time-domain methods are not affected much by the eccentricity of the orbit and may be more efficient for the case of high-eccentricity EMRIs. Therefore, time-domain methods seems to be more suitable for dealing with EMRIs these are two issues that one has to solve:

(i) The fact that one has to resolve very different physical scales (both spatial and temporal) present in the EMRI problem: those associated with the SCO and those associated with the MBH (see, e.g. [Sopuerta et al. (2005)]). In general, using a standard numerical discretization we have to resolve the gravitational typical wavelengths (comparable to

the size of the MBH) and, at the same time, scales in the vicinity of the SCO, which are crucial for evaluating the self-force. This translates in a demanding requirement of computational resources.

(ii) The fact that numerically the SCO usually is described as a point-like object. This introduces a Dirac delta distributions in its energy-momentum distribution which, in turn, induces loss of differentiability in the perturbative solutions and hence, degrades the convergence properties of the numerical algorithms used. Moreover, such a localized distribution of matter can also introduce spurious high-frequency modes that contaminate the numerical solution and, in consequence, degrade its accuracy.

Recently, there have been different proposals to improve the performance of time domain methods. Barack and Goldbourn [Barack & Golbourn (2007)] have introduced a new technique to compute the scalar field generated by a pointlike scalar charge orbiting a black hole. This technique consists in subtracting from each azimuthal mode (in the more realistic Kerr geometry the field equations are are not fully separable in the time domain and one has to unfold them in $2+1$ dimensions) of the retarded field a piece that describes the singular behavior near the particle. This is done through a careful analytical study of the scalar field near the particle [Brandt & Bruegmann (1997); Campanelli et al. (2006); Baker et al. (2006)]. On the other hand, Vega and Detweiler [Vega & Detweiler (2008)] have introduced another new method for regularizing the solution of the field equations. Their approach, tested on a simplified model of a charged particle orbiting a nonrotating black hole, regularizes the retarded field itself by identifying and removing first, in an analytical way, the singular part of the retarded field. This alternative approach to the mode-sum regularization scheme yields a finite and differentiable remainder from which the self-force can be computed. This remainder is the solution to a field equation with a nonsingular source, which avoids the problem (ii) above. Finally, Lousto and Nakano [Lousto & Nakano (2008)] have also introduced an analytical technique to remove the particle singular behaviour. Their method is global and also produces a well behaved source for the field equations.

2.3 A New Time-Domain Method

In the present work, we introduce a new time-domain scheme towards the computation of the self-force. The primary reason for undertaking this study is that, the new proposals mentioned above, Sec. 2.2, help in dealing with problem (ii), but they do not completely solve the problem (i) since the regular source terms that these new schemes produce still have associated a length scale. From the numerical point of view, this means that there are still special spatial resolution requirements associated with those source terms.
Instead of computing the GWs generated by an EMRI system, we will consider the scalar waves produced by a small scalar particle on a circular orbit around a Schwarzschild black hole. The reason for this simplification is that this model is easier to deal with mathematically but contains all the components of the gravitational EMRI problem.
The key idea of our method consists in dividing the computational domain in multiple subdomains and locate the particle in the interface between two of them (this has similarities with what was done in [Sopuerta & Laguna (2006)], in this way the length scale associated with the particle disappears. Then, the presence of the SCO/particle in the PDEs enters through the boundary conditions that communicate the solutions at the different domains.

As a consequence, we are solving homogeneous wave-type equations with smooth solutions, which avoid the problems described in (ii). Furthermore, this technique avoids the problems associated with the impact of a low differentiability of the solution in the accuracy of the numerical computations. The spatial discretization of the field equations is done by using the *PseudoSpectral Collocation* (PSC) method (see, e.g. [Boyd (2001)]), and the time evolution, uses a Runge-Kutta (RK) solver.
We will see how this special framework can provide very efficient and accurate computations in the time domain, which makes the technique amenable for the intensive computations required in the astrophysically-relevant scenarios for LISA. Regarding (i), we just need to provide the numerical resolution to describe the field near the particle, but not the particle itself, which makes the computation much more efficient.

Chapter 3

The Pseudospectral Collocation Method

Working with general relativity one deals with problems where gravity is coupled with matter sources, that is, with sets of coupled PDEs which turn out too complicated to be solved analytically. Thus, in order to handle the problem one represent functions and its derivatives numerically. In general, with spectral methods the solutions of PDEs are approximated by expanding the variables of the problem in a given basis of functions. Then, by using an appropriate criterium, we force this expansion to agree with the exact solution as we increase the number of functions included.
Suppose we have a PDE system given by:

$$L[U](x) = S(x) \qquad x \in \Omega\,, \tag{3.1}$$
$$H[U](x) = 0 \qquad x \in \partial\Omega, \tag{3.2}$$

where L is a linear operator defining the equations, H the operator defining the boundary conditions, S is the source term, and Ω denotes the domain in which the PDE is defined. The starting point in spectral methods is to approximate the solution $U(x)$ by expanding it in terms of $N+1$ basis functions $\{\phi_i\}_{i=0...N}$

$$U_N(t,x) = \sum_{i=0}^{N} a_i(t)\,\phi_i(x), \tag{3.3}$$

where $\{a_i\}_{i=0...N}$ are the spectral coefficients of the expansion. A function U_N is said to be an approximate numerical solution of (3.1) if it satisfies (3.2) and makes *small* the *residuals*:

$$R_N(t,x) = L[U_N] - S, \tag{3.4}$$

at the spacetime point (t,x). In this way, what characterizes an spectral method is essentially determined by the conditions that one imposes on the residuals in order to make them to be as close as possible to the zero in the domain Ω. Since the residual is identically zero for the exact solution, the challenge is to choose the coefficients a_i so that the residual function is minimized. As error minimization conditions, we choose to make the residual zero, at a set of points (the *collocation points*), equal in number to the spectral coefficients, that is

$$U_N(x_i) = U(x_i) \qquad i = 0, ..., N \tag{3.5}$$

This is called the *collocation* or *PseudoSpectral Collocation* method, [Boyd (2001)], and U_N is called the interpolating approximation to the function $U(x)$. On the other hand, for a set of $N+1$ points $\{x_i\}$, $i = 0, ..., N$, we can fit them by a polynomial of degree N via

$$U_N(x) = \sum_{i=0}^{N} U(x_i) C_i(x) \ , \tag{3.6}$$

which is called a *Lagrangian interpolant*, and where $C_i(x)$ are the Lagrange Cardinal functions, [Boyd (2001)], which have the property

$$C_i(X_j) = \delta_{ij} \, . \tag{3.7}$$

Consider the interval $[a, b]$ which contains x and the interpolation points, $\{x_i\}$. Thus, the error in interpolating a function $U(x)$ by its Lagrangian interpolant of degree N, $U_N(x)$, is given by

$$U(x) - U_N(x) = \frac{1}{(N+1)!} U^{(N+1)}(\xi) \prod_{i=0}^{N} (x - x_i) \ . \tag{3.8}$$

where the point ξ depends upon the function being approximated, upon N, upon x, and upon the location of the interpolation points x_i. The expression (3.8) is called *Cauchy interpolation error*. Notice that the only part of equation (3.8) that can be controlled by changing the location of the interpolation points is the polynomial

$$\prod_{i=0}^{N} (x - x_i) \ . \tag{3.9}$$

For $N+1$ arbitrary collocation points $\{x_i\}$, defined on the interval $[-1, 1]$, we can always find constants (weights), ω_i, such that for any polynomial of degree N, $f_N(x)$, the following integration rule (quadrature formula) is exact

$$\int_{-1}^{1} dx f_N(x) = \sum_{i=0}^{N} \omega_i f_N(x_i), \qquad i = 0, ..., N \ . \tag{3.10}$$

The weights, ω_i, can be found by solving the linear system obtained by imposing this formula for the different powers of x up to N. Thus, expression (3.10) is automatically fulfilled for any polynomial of degree N, which by definition are a linear combination of powers of x.
In the case that the collocation points $\{x_i\}$ are the zeros of $N+1$ orthonormal polynomial $\{\phi_i\}_{\, i=0...N}$ with respect to the weight function $\omega(x)$

$$\langle \phi_i, \phi_j \rangle = \int_{-1}^{1} dx \omega(x) \phi_i(x) \phi_j(x) = \delta_{ij} \nu_i^2 \ , \tag{3.11}$$

then, for all polynomial of at most degree $2N+1$, $U(x)$, the equation (3.10) give us the expression for the *Gauss-Jacobi integration* rule:

$$\int_{-1}^{1} dx \omega(x) U(x) = \sum_{i=0}^{N} \omega_i U(x_i), \qquad i = 0, ..., N \ , \tag{3.12}$$

where ω_i are the quadrature weights given by

$$\sum_{i=0}^{N} (x_i)^k \omega_i = \int_{-1}^{1} dx \omega(x) x^k, \qquad k = 0, ..., N \ . \tag{3.13}$$

Or alternatively by

$$\omega_i = \int_{-1}^{1} dx C_i(x) \ , \tag{3.14}$$

where $C_i(x)$ denotes the cardinal functions associated with the zeros of $\{\phi_i\}_{i=0...N}$.
The integration rule (3.12) can also be defined for a polynomial made up of a combination of $\{\phi_i\}_{i=0...N}$ giving the so called Gauss integration formulas. When the $\{x_i\}$ collocation points are the zeros of the orthonormal polynomial

$$\psi(x) = \phi_{N+1}(x) + \gamma_1 \phi_N(x) - \gamma_2 \phi_{iN-1}(x) \ , \tag{3.15}$$

where γ_1 and γ_2 are chosen so that $\psi(-1) = \psi(1) = 0$ and $U(x)$ are polynomials of at most degree $2N-1$. Then, we have a *Gauss-Lobatto Integration*
The relation of orthogonality defined for the polynomials $\{\phi_i\}_{i=0...N}$ for the continuum, (3.11), together with the Gauss integration formulas, leads us to the fact that these polynomials are still orthogona with respect the discrete inner product defined by:

$$[u, v] = \sum_{i=0}^{N} \omega_i u(x_i) v(x_j) \ , \tag{3.16}$$

that is

$$[\phi_i, \phi_j] = \sum_{i=0}^{N} \omega_i \phi(x_i) \phi(x_j) = \delta_{ij} \nu_i^2 \ . \tag{3.17}$$

Thus, from equation (3.3) we can obtain the spectral coefficients a_i, without approximation, by using the inner discrete product, [Boyd (2001)].

$$a_i = \frac{[U, \phi_i]}{[\phi_i, \phi_i]} = \frac{[U, \phi_i]}{|\phi_i|} = \frac{1}{\nu_i^2} \sum_{i=0}^{N} \omega_i U(x_i) \phi_i(x_i), \tag{3.18}$$

Hence, an inverse relation is given by

$$U(t, x_i) = \sum_{i=0}^{N} a_i(t) \, \phi_i(x). \tag{3.19}$$

Therefore, PSC methods enable one to transform easily from the physical space $\{U(x_i)\}$ to the spectral space $\{a_i\}$, as we can see from equations (3.3) and (3.19). In this way, it is possible to apply PSC methods using either the grid point values $U(x_i)$ or the series coefficients a_i as the unknowns. This fact is important because algorithms for nonlinear problems must jump back and forth between the grid point representation and the truncated series.
For example, suppose that we have a time independent solution which is approximated by a Cardinal function representation then, the physical picture approach to the solution reads

$$U_N(x) = \sum_{i=0}^{N} U(x_i) C_i(x) \ , \tag{3.20}$$

where $C_i(x)$ are the cardinal functions associated with the collocation-point grid and basis functions that we have chosen. Then, introducing this expression in (3.1), we get the following matrix problem

$$\mathbb{L}^P \cdot \mathbf{U} = \mathbf{S}, \tag{3.21}$$

where $\mathbb{L}^P$ is the matrix with components

$$L_{ij}^P = L[C_j](x_i) \ , \tag{3.22}$$

$\mathbf{U}$ is a vector with components $U_i = U(x_i)$, and $\mathbf{S}$ is the source vector with components $\mathbf{S}_i = S(x_i)$. On the other hand, the spectral picture is given by the spectral basis function representation, and the approximated solution is given by equation (3.3)

$$U_N(x) = \sum_{i=0}^{N} a_i \phi_i(x) \ . \tag{3.23}$$

Then, the spectral matrix problem is

$$\mathbb{L}^S \cdot \mathbf{a} = \mathbf{S}, \tag{3.24}$$

where $\mathbb{L}^S$ is the matrix with components

$$\mathbb{L}_{ij}^S = L[\phi_j](x_i) \ , \tag{3.25}$$

where $\mathbf{a}$ is a vector with components $\mathbf{a}_i = a_i$. Taking into account equation (3.18), the relationship between the physical and spectral pictures can be written in matrix form as follows

$$\mathbb{M} \cdot \mathbf{U} = \mathbf{a} \ , \tag{3.26}$$

which is equivalent to equation (3.18), and where $\mathbb{M}$ has components

$$M_{ij} = \frac{\phi_i(x_j)\omega_j}{[\phi_i, \phi_i]} = \frac{\phi_i(x_j)\omega_j}{\nu_i^2} \ . \tag{3.27}$$

Combining equations (3.21), (3.24) and (3.26), we can establish the following matrix relation:

$$\mathbb{L}^S \cdot \mathbb{M} = \mathbb{L}^P \ . \tag{3.28}$$

Moreover, the inverse of (3.26) is given by equation (3.19), then the components of the inverse of $\mathbb{M}$ are given by

$$M_{ij}^{-1} = \phi_j(x) \ . \tag{3.29}$$

and hence we have

$$\mathbf{U} = \mathbb{M}_{ij}^{-1} \cdot \mathbf{a} \ . \tag{3.30}$$

Therefore, we can move back and forth from one representation to another by using a square matrix, the so-called *Matrix Multiplication Transformation.*
The differentiation of equation (3.3) admits the following expansion

$$\frac{d^m U_N(x)}{dx^m}(x) = \sum_{i=0}^{N} U_N^{(m)}(x_i)\phi_i(x) \ , \tag{3.31}$$

where $\{x_i\}$ is the collocation grid. The coefficients $U_N(x_i)$ and $U_N^{(m)}(x_i)$ can be related through a *differentiation matrix* (of order m), D_{ij}^m, as follows

$$U_N^m(x_i) = \sum_{j=0}^{N} D_{ij}^{(m)} U_N(x_j) \ , \tag{3.32}$$

where the D_{ij}^m matrix can be obtained in terms of the associated Cardinal functions $C_i(x)$ as reads

$$D_{ij}^{(m)} = \frac{d^m C_j}{dx^m}(x_j) \, . \tag{3.33}$$

In order to perform some operations that involve change of representation it is useful to change representation by means of a discrete Fourier transform using a Fast-Fourier Transform (FFT) algorithm (see Sec. 4.3). Then, the number of computations required for a change of representation scales as $\sim N \ln N$ with the number of collocation points. Moreover, differentiation is easier in the spectral representation, so we can transform from the physical to the spectral representation, compute derivatives there, and finally transform back to the physical representation.

3.1 Some Properties of the Chebyshev Polynomials

When the solution of our PDE problem is searched in a finite-dimensional subspace of some given Hilbert space in terms of the equation (3.3), then the functions $\{\phi_i\}_{i=0\ldots N}$ are called trial functions, [Grandclement & Novak (2009)], which for spectral and pseudospectral methods are global smooth functions on Ω. In this work we use Chebyshev polynomials, $\{T_n\}$, as basis functions

$$T_n(X) = \cos\left(n \cos^{-1}(X)\right) , \tag{3.34}$$

which are defined in the domain $X \in [-1, 1]$, with $|T_n(X)| \leq 1$, and n is the degree of the polynomial.
Of all polynomials of degree $N+1$, P_{N+1}, which have leading coefficient (coefficient of X^{N+1}) equal to unity, the Chebyshev polynomial T_{N+1} is the unique which has the smallest maximum on the interval $[-1, 1]$ [Boyd (2001)]:

$$\max \left\| P_{N+1}(X) \right\| \geq \max \left\| \frac{T_{N+1}(X)}{2^N} \right\| = \frac{1}{2^N} \, . \tag{3.35}$$

Then if $\{X_i\}$ are the roots of T_{N+1}, we can write equation (3.9) as

$$2^N \, T_{N+1}(X) = \prod_{i=0}^{N} (X - X_i) \, . \tag{3.36}$$

where $X \in [-1, 1]$. In this way, we can always map the interval $[a, b]$ to the interval $[-1, 1]$ and find optimal interpolation points as the roots of the Chebyshev polynomial of order $N+1$. In other words, to minimize the Cauchy remainder, the polynomial (3.9) has to be proportional to T_{N+1}.
Another property of the Chebyshev polynomials is that they are orthogonal in the *continuum*:

$$(T_n, T_m) = \int_{-1}^{1} \frac{dX}{\sqrt{1 - X^2}} T_n(X) \, T_m(X) = \frac{\pi c_n}{2} \delta_{nm} \, , \tag{3.37}$$

where the coefficients c_n are given by

$$c_n = \begin{cases} 2 & \text{for } n = 0 \, , \\ 1 & \text{otherwise} \, . \end{cases} \tag{3.38}$$

On the other hand, there is also a correspondence between Chebyshev series an Fourier series given by the map

$$X: \qquad [0,2\pi] \longrightarrow \quad [-1,1] \tag{3.39}$$

$$\theta \longrightarrow \qquad X(\theta) = \cos(\theta), \tag{3.40}$$

so that

$$T_n(X) = \cos\left(n\theta\right), \tag{3.41}$$

and we have the following equivalence

$$U(X) = \sum_{n=0}^{\infty} a_n T_n(X) \quad \Longleftrightarrow \quad U(\cos\theta) \sum_{n=0}^{\infty} a_n \cos(n\theta). \tag{3.42}$$

Then, an expansion in Chebyshev polynomials can be mapped to a cosine expansion. Notice that for the case of Fourier and Chebyshev series, the matrix multiplication transformation, defined in equation (3.30), can be carried out by means of the *Fast Fourier Transform* (FFT) algorithm.

In this work, the spatial discretization of the PDEs is performed by means of the PSC method, where the set of collocation points are the extrema of the Chebyshev polynomials, together with the end points $X = \pm 1$. Hence, our grid is made out of the zeros of the following polynomial

$$(1 - X^2) T'_N(X) = 0\,, \tag{3.43}$$

where the prime indicates differentiation with respect to X, and the zeros can be written as follows:

$$X_i = -\cos\left(\frac{\pi\, i}{N}\right) \quad (i = 0, 1, \ldots, N)\,. \tag{3.44}$$

These points form, in the interval $[-1,1]$, a *Chebyshev-Lobatto* collocation grid. Where the distance of the collocation points near the middle of the interval goes as N^{-1} whereas near the ends of the interval goes as N^{-2}. Therefore, the density of collocation points is bigger at the ends of the interval than in the middle of it. The cardinal functions associated with the Chebyshev-Lobatto collocation grid are

$$\mathcal{C}_i(X) = \frac{(1 - X^2) T'_N(X)}{(1 - X_i^2)(X - X_i) T''_N(X_i)} \qquad i = 0, \ldots, N\,. \tag{3.45}$$

Once this set of collocation points is adopted, and taking into account the properties of the Gauss-Lobatto-Chebyshev quadratures mentioned above, the Chebyshev polynomials have another orthogonality relation, this time in the *discrete*, in the following sense ($n, m = 0, \ldots, N$):

$$[T_n, T_m] = \sum_{i=0}^{N} w_i\, T_n(X_i)\, T_m(X_i) = \nu_n^2\, \delta_{nm}\,, \tag{3.46}$$

where w_i are the weights associated with the Chebyshev-Lobatto grid, $w_i = \pi/(N\,\bar{c}_i)$, and where the $\bar{c}_i$'s are normalization coefficients given by

$$\bar{c}_i = \begin{cases} 2 & \text{for } i = 0, N\,, \\ 1 & \text{otherwise}\,. \end{cases} \tag{3.47}$$

Finally, the constants ν_n in (3.46) are given by $\nu_n^2 = \pi \bar{c}_n / 2$.

3.2 Spectral Filter

In order to reduce the spurious (of non-physical origin) high-frequency components of our numerical solutions, we apply a spectral filter of the exponential type to the solution after every time step, that is, after every full RK step. The scheme for the action of the spectral filter is

$$\{\boldsymbol{U}_i\} \overset{FFT}{\longrightarrow} \{\boldsymbol{a}_n\} \overset{\text{Filter}}{\longrightarrow} \{\tilde{\boldsymbol{a}}_n\} \overset{FFT}{\longrightarrow} \{\tilde{\boldsymbol{U}}_i\}\,, \tag{3.48}$$

where $\{\boldsymbol{U}_i\}$ are the values of the solutions at the collocation points after the RK step; $\{\boldsymbol{a}_n\}$ are their corresponding spectral components; $\{\boldsymbol{b}_n\}$ are the filtered spectral components; and $\{\tilde{\boldsymbol{U}}_i\}$ are the filtered values of the solution at the collocation points. The exponential filter is defined by its action on the spectral coefficients $\{\boldsymbol{a}_n\}$ to yield the spectral coefficients $\{\boldsymbol{b}_n\}$. This action is given by

$$\tilde{\boldsymbol{a}}_n = \sigma\left(\frac{n}{N}\right)\,\boldsymbol{a}_n\,, \tag{3.49}$$

where $\sigma(n/N)$ is the exponential filter

$$\sigma\left(\frac{n}{N}\right) = \begin{cases} 1 & \text{for } 0 \leqslant n \leqslant N_c\,, \\ \exp\left[-\alpha(\frac{n-N_c}{N-N_c})^{\gamma}\right] & \text{for } N_c < n \leq N\,, \end{cases} \tag{3.50}$$

where N_c is the cut-off mode number, γ is the order of the filter (typically chosen to be of the order of the number of collocation points, N), and α is the machine accuracy parameter, which is related to the machine accuracy, ϵ_M, by $\alpha = -\ln \epsilon_M$. For a 32 bit machine and double precision we have: $\epsilon_M = 2^{-52} \;\rightarrow \alpha \simeq 36.0437$.

Chapter 4

A New Time-Domain Framework for Simulations of EMRIs

In this chapter we describe the simplified model of an EMRI that we have studied. This model corresponds to a scalar particle which orbits a nonrotating black hole in circular geodesics. Later, in Sec. 4.2, we introduce a new time-domain method to solve the equations of our problem and also to compute the self-force from the solution.

4.1 A Simple Model: A Charged Scalar Particle Orbiting a Nonrotating Massive Black Hole

In this section we are going to describe a new technique for the computation of the self-force. We focus in the particular case of a charged scalar particle in circular geodesics around a non-rotating MBH. In this simplified model, which contains all the ingredients of the gravitational EMRI problem, the spacetime metric is not dynamical, that is, it is fixed. Since we are considering non-rotating BHs, we take the metric to be Schwarzschild one, which can be written as follows:

$$ds^2 = f(-dt^2 + dr^{*2}) + r^2 d\Omega^2 \,,\; d\Omega^2 = d\theta^2 + \sin^2\theta d\varphi^2 \,, \tag{4.1}$$

where $(x^\mu) = (t, r, \theta, \varphi)$ are the so-called Schwarzschild coordinates, $f(r) = 1 - 2M/r$ (where M is the BH mass), and r^* is the *tortoise* coordinate, given by:

$$r^* = r + 2M \ln\left(\frac{r}{2M} - 1\right) \,. \tag{4.2}$$

In this geometry we assume there is a test particle with scalar charge q, associated to a scalar field $\Phi(x^\mu)$. This particle is orbiting the BH, and in doing so generates scalar field Φ, which in turn influences the particle trajectory. That is, the particle motion is affected by the field created by itself. In this way, this model contains all the ingredients of the gravitational case, in which the particle motion is influenced by its own gravitational field as it happens with EMRIs.

The equation for the scalar field is then (see, e.g. [Poisson (2004)]):

$$\mathrm{g}^{\alpha\beta}\nabla_\alpha\nabla_\beta\Phi(x) = -4\pi\rho \,, \tag{4.3}$$

$$\rho = -4\pi q \int_\gamma d\tau\, \delta_4(x, z(\tau)) \,, \tag{4.4}$$

that is, a wave-type equation with a source term that describes the particle energy density due to its scalar charge. In this equation, the spacetime metric $g_{\mu\nu}$ is the Schwarzschild metric (4.1), ∇_μ denotes the associated canonical connection; τ denotes proper time associated with the particle along its timelike worldline γ; and $\delta_4(x, x')$ is the invariant Dirac functional in Schwarzschild spacetime, which is defined by the relations

$$\int_\gamma d^4x\sqrt{-g(x)}f(x)\delta_4(x,x') = f(x')\,, \tag{4.5}$$

and the equivalent one for the other argument. In this relation, g denotes the metric determinant. Taking into account the properties of $\delta_4(x, x')$, it follows that the source term in the scalar field equation (4.4) only has support on the particle worldline γ.

Denoting the trajectory of the particle by $x^\mu = z^\mu(\tau)$, the equations of motion for the particle that one would obtain from energy-momentum conservation are:

$$m\frac{du^\mu}{d\tau} = F^\mu = q(g^{\mu\nu} + u^\mu u^\nu)\nabla_\nu\Phi\,, \quad u^\mu = \frac{dz^\mu}{d\tau}\,, \tag{4.6}$$

where m and u^μ are the particle mass and 4-velocity, respectively. However, this expression is a formal one due to the fact that the force F^μ diverges on the particle worldline γ (see [Quinn (2000)] for a derivation of the *regularized* equations of motion). An analysis of the solutions of (4.4) and (4.6) reveals (see for details [Poisson (2004)]) that the gradient of the field, $\nabla_\mu\Phi$, can be split into two parts [Detweiler & Whiting (2003)]: A singular piece, $\Phi^{\rm S}$, which contains the singular structure of the field and satisfies the same field equation

$$g^{\alpha\beta}\nabla_\alpha\nabla_\beta\Phi^{\rm S} = -4\pi\rho\,, \tag{4.7}$$

and a regular part, $\Phi^{\rm R} = \Phi - \Phi^{\rm S}$, which satisfies an homogeneous wave equation

$$g^{\alpha\beta}\nabla_\alpha\nabla_\beta\Phi^{\rm R} = 0\,, \tag{4.8}$$

and which is solely responsible of the deviation of the particle from geodesic motion around the BH,

$$m\frac{du^\mu}{d\tau} = q(g^{\mu\nu} + u^\mu u^\nu)\nabla_\nu\Phi^{\rm R}\,. \tag{4.9}$$

$\Phi^{\rm R}$ is the associated part containing the tail of the scalar field, and equation (4.9) is the analogous equation to the *MiSaTaQuWa* equation which describes the motion of a small mass in general relativity (the gravitational case), taking into account the leading order self-force effects (see [Mino et al. (1997); Quinn & Wald (1997)]), and

$$F^{\rm R}_\mu = q(g^{\mu\nu} + u^\mu u^\nu)\nabla_\nu\Phi^{\rm R} \tag{4.10}$$

is the *self-force* acting on the particle.
In order to solve the equation for the scalar field (4.4) it is very convenient to take advantage of the spherical symmetry of the Schwarzschild spacetime, and decompose Φ in scalar spherical harmonics, $Y^m_\ell(\theta,\varphi)$ (see Appendix A.1),

$$\Phi(x) = \sum_{\ell=0}^{\infty}\sum_{m=-\ell}^{\ell}\Phi^m_\ell(t,r)Y^m_\ell(\theta,\varphi)\,, \tag{4.11}$$

where the harmonic numbers (ℓ, m) take the usual values: $\ell = 0, 1, 2, ..., \infty$, and $m = -\ell, -\ell + 1, ..., \ell - 1, \ell$. Notice that to compute the self-force we are considering geodesic motion of the

particle, which in Schwarzschild takes place on a plane. Then, we can assume, without loss of generality, that the plane is given by $\theta = \pi/2$. We will also parameterize the motion of the particle in terms of the coordinate time t, instead of proper time τ. That is, the particle worldline, γ, will be given by $(t, r_p(t), \pi/2, \varphi_p(t))$. Taking this into account, we can introduce the expansion (4.11) into the scalar field equation (4.4) and find that the equations for the different harmonic coefficients $\Phi^m_\ell(t,r)$ decouple and have the form of a 1+1 wave-type equation:

$$\left\{-\frac{\partial^2}{\partial t^2} + \frac{\partial^2}{\partial r^{*2}} - V_\ell(r)\right\}(r\Phi^m_\ell) = S^m_\ell \delta(r - r_p(t))\,, \tag{4.12}$$

where $V_\ell(r)$ is the Regge-Wheeler potential for scalar fields on the Schwarzschild geometry, given by

$$V_\ell(r) = f(r)\left[\frac{\ell(\ell+1)}{r^2} + \frac{2M}{r^3}\right], \tag{4.13}$$

and S^m_ℓ is the coefficient of the singular source term generated by the particle:

$$S^m_\ell = -\frac{4\pi q f^2(r_p)}{r_p u^t}\,\bar{Y}^m_\ell(\frac{\pi}{2}, \varphi_p)\,, \tag{4.14}$$

where an overbar denotes complex conjugation. On a hypersurface $\{t = t_o\}$, we can prescribe the initial data for Φ^m_ℓ like

$$({}_o\Phi^m_\ell,\ {}_o\dot{\Phi}^m_\ell) = (\Phi^m_\ell(t_o, r)\ ,\ \partial_t\Phi^m_\ell(t_o, r))\,, \tag{4.15}$$

and then find the correspondent solution. Hence, as Φ satisfies a wave equation, a unique solution to the problem exist which depends continuously on the problem initial data, that is the problem is well-posed. Notice that the solution found in this way corresponds to the (ℓ, m) contribution to the full retarded solution. Moreover, this solution will be finite and continuous at the particle location, but it will not be differentiable at that point, in the sense that the radial derivative from the left and from the right of the particle yields different values. Furthermore, the sum of the multipole coefficients over ℓ will diverge at the particle location. This last feature can be fixed by extracting, multipole by multipole, the singular part of the scalar field (see Sec. 1).
Since we are interested in regularizing the self-force, which is defined only at the particle location, we introduce first a multipolar decomposition of the gradient of the scalar field

$$\Phi^\ell_\alpha(x^\mu) = \nabla_\alpha \sum_{m=-\ell}^{\ell} \Phi^m_\ell(t,r)\, Y^m_\ell(\theta,\varphi)\,, \tag{4.16}$$

so that the gradient of the retarded field is given by

$$\Phi_\alpha(x^\mu) = \sum_{\ell=0}^{\infty} \Phi^\ell_\alpha(x^\mu)\,. \tag{4.17}$$

Obviously, $\Phi_\alpha(x^\mu)$ also diverges at the particle worldline although the Φ^ℓ_α are finite.

The gradient of Φ, and hence the self-force, can be regularized by splitting the full retarded field by analytically identifying and removing the singular part of the retarded field, [Vega & Detweiler (2008)]. This alternative approach to the mode-sum regularization scheme yields

a finite, differentiable remainder from which the self-force can be computed. Summarizing, the self-force can be regularized by splitting the full retarded field into a singular part and a regular part (see, for instance, [Detweiler & Whiting (2003); Poisson (2004)]), such that they satisfy equations (4.7)-(4.9). In this manner, on the particle location, the regular part of the gradient of the scalar field will be given by

$$\Phi^R_\alpha(z^\mu(\tau)) = \lim_{x^\mu \to z^\mu(\tau)} \sum_{\ell=0}^{\infty} \left(\Phi^\ell_\alpha(x^\mu) - \Phi^{S,\ell}_\alpha(x^\mu) \right) . \tag{4.18}$$

The singular field Φ^S is known in a neighborhood of the particle worldline. In particular, the multipoles of the singular part of the gradient of the scalar field at the particle worldline are given by [Barack & Ori (2000); Barack (2000, 2001); Barack et al. (2002); Barack & Ori (2002, 2003); Mino et al. (2003)]:

$$\lim_{x^\mu \to z^\mu(\tau)} \Phi^{S,\ell}_\alpha = q \left[\left(\ell + \frac{1}{2} \right) A_\alpha + B_\alpha + \frac{C_\alpha}{\ell + \frac{1}{2}} - \frac{2\sqrt{2} D_\alpha}{(2\ell - 1)(2\ell + 3)} + ... \right] , \tag{4.19}$$

where A_α, B_α, C_α, D_α, ... are called the regularization parameters [Barack et al. (2002); Barack & Ori (2002, 2003); Mino et al. (1997)]. They are independent of ℓ, but depend on the particle dynamics. The singular part corresponds to the first three terms which lead to quadratic, linear, and logarithmical divergences. The remaining terms form a convergent series that does not contribute to the self-force (each of them). In our approximate calculations, we maintain the D_α term as it accelerates the convergence of the series as we increase the number of multipoles included [Detweiler et al. (2003); Haas & Poisson (2006)]. For the case of interest of this work, circular geodesics, the non-vanishing regularization parameters are A_r, B_r, and D_r [Barack & Ori (2002, 2000); Detweiler et al. (2003)], which can be written as follows:

$$A_r = -\frac{\sigma_p}{r_p^2} \frac{\sqrt{1 - 3M/r_p}}{1 - 2M/r_p} , \tag{4.20}$$

$$B_r = -\frac{1}{r_p^2} \sqrt{\frac{1 - 3M/r_p}{1 - 2M/r_p}} \left[F_{1/2} - \frac{1 - 3M/r_p}{2(1 - 2M/r_p)} F_{3/2} \right] , \tag{4.21}$$

$$\begin{aligned} D_r &= \frac{1}{r_p^2} \sqrt{\frac{2(1 - 2M/r_p)}{1 - 3M/r_p}} \left\{ -\frac{M}{2r_p} \frac{1 - 2M/r_p}{1 - 3M/r_p} F_{-1/2} - \frac{(1 - M/r_p)(1 - 4M/r_p)}{8(1 - 2M/r_p)} F_{1/2} \right. \\ &+ \left. \frac{(1 - 3M/r_p)(5 - 7M/r_p - 14M^2/r_p^2)}{16(1 - 2M/r_p)^2} F_{3/2} - \frac{3(1 - 3M/r_p)^2(1 + M/r_p)}{16(1 - 2M/r_p)^2} F_{5/2} \right\} , \end{aligned} \tag{4.22}$$

where σ_p is a sign that takes the value $+1$ when the limit in equation (4.19) is performed from the *right* ($r \geq r_p$) and -1 when the limit is performed from the *left* ($r \leq r_p$), see Appendix A.2. Since the only non-vanishing component of the regularization coefficients is the radial one, this is the only component of the self-force that is actually singular, and hence the only one to be regularized. In this way the regularized self-force is:

$$F^R_\alpha = q \, \Phi^R_\alpha(z^\mu(\tau)) . \tag{4.23}$$

4.2 Mathematical Formulation

We are going to introduce the mathematical developments needed in order to compute the self-force by numerical algorithms, based on the PSC method. The first we are going to discuss is the particular formulation that we have implemented numerically. Since our numerical framework deals with multiple domains, it is useful to adopt a first-order formulation of the scalar field equation. The main reason is that first-order formulations of PDEs can be adapted to the hyperbolic character of the underlying equation and hence, they are suitable for a correct communication between domains. In this regard, we perform a first-order reduction of (4.12) by introducing the following new variables

$$\psi^m_\ell(t,r) = r\,\Phi^m_\ell(t,r)\,, \tag{4.24}$$
$$\phi^m_\ell(t,r) = \partial_t\psi^m_\ell(t,r)\,, \tag{4.25}$$
$$\varphi^m_\ell(t,r) = \partial_{r^*}\psi^m_\ell(t,r)\,. \tag{4.26}$$

The evolution equations for a given harmonic, (ℓ,m), $\boldsymbol{U}=(\psi^m_\ell,\phi^m_\ell,\varphi^m_\ell)$, written in matrix form read:

$$\partial_t\boldsymbol{U} = \mathbb{A}\cdot\partial_{r^*}\boldsymbol{U} + \mathbb{B}\cdot\boldsymbol{U} + \boldsymbol{S}\,, \tag{4.27}$$

where

$$\mathbb{A} = \begin{pmatrix} 0 & 0 & 0 \\ 0 & 0 & 1 \\ 0 & 1 & 0 \end{pmatrix}\,,\quad \mathbb{B} = \begin{pmatrix} 0 & 1 & 0 \\ -V_\ell & 0 & 0 \\ 0 & 0 & 0 \end{pmatrix}\,, \tag{4.28}$$

and

$$\boldsymbol{S} = \left(0, -\frac{S^m_\ell}{f(r_p)}\delta(r^*-r^*_p(t)), 0\right)\,. \tag{4.29}$$

It can be seen that (4.27) is a first-order symmetric hyperbolic system of PDEs, with characteristic structure described by the matrix $\mathbb{A}$.
Given that discontinuities in the solution are only allow across characteristics and due to the singular character of the source, some of our variables will have jumps across the radial particle location. We are going to study these jumps using the formulation just introduced. To approach this question it is convenient to divide the spatial domain (the radial direction as parametrized by the coordinate r^*) into two disjoint regions, one to the left of the particle ($r^* < r^*_p(t)$), and one to the right of the particle ($r^* > r^*_p(t)$). Then, we can write the solution of the equations (4.27) in the form (see also [Sopuerta & Laguna (2006)]):

$$\boldsymbol{U} = \boldsymbol{U}_-(t,r)\Theta(r^*_p(t)-r^*) + \boldsymbol{U}_+(t,r)\Theta(r^*-r^*_p(t))\,, \tag{4.30}$$

where Θ denotes the Heaviside step function. Introducing (4.30) into (4.27) we can derive the jump across the particle location, defined as

$$[\,\lambda\,]_p = \lim_{r^*\to r^*_p}\lambda_+(t,r^*) - \lim_{r^*\to r^*_p}\lambda_-(t,r^*)\,. \tag{4.31}$$

For the different variables of our problem. We find the following result:

$$[\,\psi^m_\ell\,]_p = 0\,,\quad [\,\phi^m_\ell\,]_p = 0\,,\quad [\,\varphi^m_\ell\,]_p = \frac{S^m_\ell}{f(r_p)}\,. \tag{4.32}$$

These are the conditions we have to impose in our numerical evolution algorithm. In practice, these conditions have to be imposed on the *characteristic* fields. In our problem there are two different types of characteristics: (i) The $\{t = \text{const.}\}$ surfaces, and (ii) the null surfaces $\{t \pm r^* = \text{const.}\}$. The associated characteristic fields are ψ^m_ℓ, and $\phi^m_\ell \mp \varphi^m_\ell$, respectively. Finally, our system of equations has to be complemented with initial conditions and boundary conditions. The initial conditions, since we are dealing with a first-order system of PDEs, consist in prescribing $\boldsymbol{U}_o(r^*) = \boldsymbol{U}(t = t_o, r^*)$. We need boundary conditions at the ends of the spatial domain. The physical spatial domain is $r^* \in (-\infty, +\infty)$, here $r^* \to -\infty$ corresponds to the horizon location, where $r^* \to +\infty$ corresponds to spatial infinity. In our numerical computations we will take a *truncated* domain: $r^* \in [r^*_{\rm H}, r^*_{\rm I}]$ (see figure 4.1) and therefore we need to prescribe outgoing boundary conditions at the ends of that domain (also called *absorbing* boundary conditions). As an approximation we take the conditions that are exact for the case in which there is no potential, that is [restoring the (ℓ, m) indices]

$$\phi^m_\ell(t, r^*_{\rm H}) - \varphi^m_\ell(t, r^*_{\rm H}) = 0\,, \tag{4.33}$$

$$\phi^m_\ell(t, r^*_{\rm I}) + \varphi^m_\ell(t, r^*_{\rm I}) = 0\,. \tag{4.34}$$

This is the leading approximation for the outgoing boundary conditions. They can be improved by analyzing the solution near $r^* \to \pm\infty$. However, we can always take values of $(r^*_{\rm H}, r^*_{\rm I})$ such that the boundaries are not in causal contact with the particle location, avoiding contamination of the solution due to propagation of unphysical modes from the boundaries.

4.3 Using the PseudoSpectral Collocation Method

In order to solve for the PDEs that describe the scalar field, equations (4.27), we use the PSC to discretize in space. Once this is done, we obtain a system of ordinary differential equations (ODEs) that can be solved by using the method of lines applying a convenient ODE solver. For computational reasons, that will be discussed later, we split the computational domain, $\Omega = [r^*_H, r^*_I]$, into a number of D sub-domains:

$$\Omega = \bigcup_{a=1}^{D} \Omega_a\,, \quad \Omega_a = \left[r^*_{a,L}, r^*_{a,R}\right]\,, \tag{4.35}$$

where $r^*_{a,L}$ and $r^*_{a,R}$ are the left and right boundaries of the subdomain Ω_a. They are disjoint subdomains, that is $r^*_{a-1,R} = r^*_{a,L}$ (see figure 4.1).

We apply the PSC method to each subdomain, in the sense that our variables have different expansions in Chebyshev polynomials in each subdomain. These different expansions are related by using appropriate boundary conditions that we discuss in Sec. 4.4. To apply the PSC method to each subdomain, we map the physical subdomain Ω_a $(a = 1, \ldots, D)$ to the spectral domain, $[-1, 1]$, using a linear mapping $X_a : \left[r^*_{a,L}, r^*_{a,R}\right] \longrightarrow [-1, 1]$, with

$$r^* \longrightarrow X_a(r^*) = \frac{2r^* - r^*_{a,L} - r^*_{a,R}}{r^*_{a,R} - r^*_{a,L}}\,. \tag{4.36}$$

The inverse correspondence is another linear mapping, $r^*|_{\Omega_a} : [-1, 1] \longrightarrow \left[r^*_{a,L}, r^*_{a,R}\right]$, with

$$X \longrightarrow r^*(X)|_{\Omega_a} = \frac{r^*_{a,R} - r^*_{a,L}}{2} X + \frac{r^*_{a,L} + r^*_{a,R}}{2}\,. \tag{4.37}$$

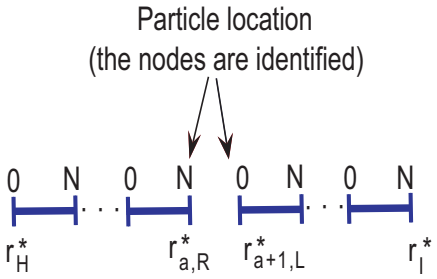

Figure 4.1: The figure shows the structure of the one-dimensional spatial grid, the division in subdomains and the location of the particle at the interface between two of them. The boundaries of the domain have coordinates $r^*_{\rm H}$ (this coordinate will have a finite value and is meant to approach the BH horizon at $r^* = -\infty$) and $r^*_{\rm I}$ (this coordinate will have too a finite value and is meant to approach spatial infinity at $r^* = +\infty$). The particle is at the boundaries of two different boundaries (which are identified), which have coordinates $r^*_{a,R}$ and $r^*_{a+1,L}$ that satisfy the relation (4.45).

We arrange the variables of our problem in a vector, $\boldsymbol{U}$. Then, at a given subdomain Ω_a $(a = 1, \ldots, D)$, it has the following spectral expansion, equation (3.19):

$$\boldsymbol{U}_N(t, r^*) = \sum_{n=0}^{N} \boldsymbol{a}_n(t)\, T_n(X_a(r^*))\,, \tag{4.38}$$

where the $\boldsymbol{a}_n$ are (time-dependent) vectors that contain the spectral coefficients of the expansion of our variables. The physical expansion of $\boldsymbol{U}$ looks as follows:

$$\boldsymbol{U}_N(t, r^*) = \sum_{i=0}^{N} \boldsymbol{U}_i(t)\, \mathcal{C}_i(X_a(r^*))\,, \tag{4.39}$$

where $\mathcal{C}_i(X)$ are the *cardinal* functions [Boyd (2001)] associated with our choice of the Chebyshev polynomials as basis functions and the Lobatto-Chebyshev grid as collocation points. Regarding the property of cardinal functions (3.7), the time-dependent (vector) coefficients, $\{\boldsymbol{U}_i\}$, of the expansion (4.39) are the values of our variables at the collocation points

$$\boldsymbol{U}(t, r^*(X_i)) = \boldsymbol{U}_i(t)\,. \tag{4.40}$$

These are the variables that one looks for in the PSC method. Hence, the spectral (4.38) and physical (4.39) representations are related via a matrix transformation. The computations (float-point operations) required to change representation scale, with the number of collocation points, as N^2, as it can be deduced from the fact that it is a matrix transformation. However, using the change of spectral coordinate given in equation (3.42), we can perform the change of representation by means of a discrete Fourier transform using a Fast-Fourier Transform (FFT) algorithm. In our numerical codes, we use the routines of the FFTW library [Frigo & Johnson (2005)]. Then, the number of computations required for a change of representation scales as $\sim N \ln N$ with the number of collocation points.
Changing between representations is useful in order to perform some operations. For instance, differentiation is easier in the spectral representation, so we can transform from the physical to the spectral representation, compute derivatives there, and finally transform back to the physical representation. In the case of a Chebyshev PSC method, the differentiation process can be described by the following scheme

$$\partial_{r^*} : \{\boldsymbol{U}_i\} \overset{FFT}{\longrightarrow} \{\boldsymbol{a}_n\} \overset{\partial_{r^*}}{\longrightarrow} \{\boldsymbol{b}_n\} \overset{FFT}{\longrightarrow} \{(\partial_{r^*}\boldsymbol{U})_i\}\,, \tag{4.41}$$

where $\{\boldsymbol{b}_n\}$ are the spectral coefficients associated with the spatial derivative, and their relation to the coefficients of the variables, $\{\boldsymbol{a}_n\}$, is given by

$$\boldsymbol{b}_N = \boldsymbol{b}_{N-1} = 0\,, \tag{4.42}$$

$$\boldsymbol{b}_{n-1} = \frac{1}{c_n}\left\{2n\boldsymbol{a}_n + \boldsymbol{b}_{n+1}\right\} \;\; (n = N-1, \ldots, 1)\,, \tag{4.43}$$

In the PSC method, we find a discretization of our system of equations (4.27) by imposing them at every collocation point. In practice, this is done by introducing the expansion (4.39) into the equations (4.27), and then we evaluate the result at every collocation point of our Chebyshev-Lobatto grid (3.44). We obtain a system of ODEs for the variables $\{\boldsymbol{U}_i(t)\}$

$$\dot{\boldsymbol{U}}_i = \mathbb{A}\cdot(\partial_{r^*}\boldsymbol{U})_i + \mathbb{B}\cdot\boldsymbol{U}_i + \boldsymbol{S}_i\,, \tag{4.44}$$

where the dot denotes differentiation with respect to the time coordinate t, and $(\partial_{r^*}\boldsymbol{U})_i$ has to be interpreted according to the scheme in equation (4.41).

4.4 Evolution Algorithm

In this section we discuss the details of the time evolution of the discrete equations we derived in the previous section. In particular, we describe how to introduce the particle in the multi-domain PSC method that we propose. The main argument is the following: If we put the particle inside one of the subdomains Ω_a we are introducing in the equations (4.27) a singular term that, in the case of a scalar charged particle, will produce solutions that are not differentiable (in the sense that the derivative with respect to r^* is not single valued at the particle location). That is, our solution will not be smooth and hence we cannot expect the PSC method to converge exponentially to the true solution. That would spoil one of the main motivations for using this numerical technique, that is, the accuracy that the PSC method provides. To avoid this (and this is part of the reason for using a multi-domain scheme) we put the particle at the interface between two subdomains. If the subdomains are Ω_a and Ω_{a+1}, we have:

$$r^*_p = r^*_{a,R} = r^*_{a+1,L}\,. \tag{4.45}$$

Since we have restricted ourselves to the case of circular orbits, once the grid has been set we do not need to change it during the evolution. In the case of generic orbits, in order to maintain the particle at the interface between two subdomains we have either to make a coordinate change or implement a moving grid scheme. We discuss this further in Sect. 6.

For each subdomain Ω_a $(a = 1, \ldots, D)$, we evolve the set of ODEs (4.44) independently. Since we are locating the particle at the interface between two subdomains, the last term in (4.44), $\boldsymbol{S}$, does not appear. This term is the source term that accounts for the particle's energy density [see equation (4.14)]. The main implication of this setup is that we have to solve the homogeneous field equations, which are equations with smooth solutions and hence, the advantages of the PSC method are preserved. Then, in our framework, the contributions of the particle to the solution appear as boundary conditions between the subdomains. In summary, we evolve the (homogeneous) field equations for each subdomain independently and connect their solutions by boundary conditions at the interfaces. The equations are evolved using a Runge-Kutta (RK) solver (see [Butcher (2008); Press et al. (1992)]), typically a RK4 algorithm.

The key point in the evolution is the imposition of boundary conditions at the interfaces between subdomains. There are two possible situations for a given interface: (i) The particle is not there. In this case we only have to impose the continuity of the solution [that would correspond to imposing the junction conditions given in equation (4.32) with zero right-hand sides]. (ii) The particle is there. In this case we have to impose the junction conditions in equation (4.32) where S_ℓ^m is given in equation (4.14). In order to impose these boundary conditions at the interfaces between subdomains in a dynamical way we use *penalty* terms.
The penalty method is a well-known technique and has been applied to several numerical schemes to solve PDEs (for the PSC method, see [Hesthaven (2000)] and references therein). It is relatively simple to implement it for elliptic-type problems, that is, for problems that do not require evolution *in time*. For time-dependent problems, it can be also implemented but not always the result is numerically stable. In our framework, the implementation of the penalty method goes as follows: First, let us consider the two domains around the particle's location, say Ω_a and Ω_{a+1}, so that equation (4.45) holds. Then, let us consider the solutions at these two subdomains, $\boldsymbol{U}_a$ and $\boldsymbol{U}_{a+1}$. The equations for the inner points are just equations (4.44), and the equations for the nodes at the interface between these subdomains, $r^*_{a,R}$ and $r^*_{a+1,L}$ (which are identified), are modified in the following way: For the subdomain Ω_a (we have simplified the notation by dropping the harmonic indices ℓ and m)

$$\partial_t \psi_{a,R} = \phi_{a,R} - \tau_\psi^{a,R} \left[\psi_{a,R} - \psi_{a+1,L}\right] , \tag{4.46}$$

$$\begin{aligned} \partial_t \phi_{a,R} &= \partial_{r^*} \varphi_{a,R} - V_p\, \psi_{a,R} - \frac{\tau_\phi^{a,R}}{2} \left[\phi_{a,R} + \varphi_{a,R} - [\varphi]_p \right. \\ &- \left. (\phi_{a+1,L} + \varphi_{a+1,L})\right] , \end{aligned} \tag{4.47}$$

$$\begin{aligned} \partial_t \varphi_{a,R} &= \partial_{r^*} \phi_{a,R} - \frac{\tau_\varphi^{a,R}}{2} \left[\phi_{a,R} + \varphi_{a,R} \right. \\ &- \left. (\phi_{a+1,L} + \varphi_{a+1,L}) - [\varphi]_p\right] , \end{aligned} \tag{4.48}$$

and for the subdomain Ω_{a+1}

$$\partial_t \psi_{a+1,L} = \phi_{a+1,L} - \tau_\psi^{a+1,L} \left[\psi_{a+1,L} - \psi_{a,R}\right] , \tag{4.49}$$

$$\begin{aligned} \partial_t \phi_{a+1,L} &= \partial_{r^*} \varphi_{a+1,L} - V_p\, \psi_{a+1,L} - \frac{\tau_\phi^{a+1,L}}{2} \left[\phi_{a+1,L} \right. \\ &- \left. \varphi_{a+1,L} - (\phi_{a,R} - \varphi_{a,R}) - [\varphi]_p\right] , \end{aligned} \tag{4.50}$$

$$\begin{aligned} \partial_t \varphi_{a+1,L} &= \partial_{r^*} \phi_{a+1,L} - \frac{\tau_\varphi^{a+1,L}}{2} \left[\phi_{a+1,L} - \varphi_{a+1,L} \right. \\ &- \left. (\phi_{a,R} - \varphi_{a,R}) - [\varphi]_p\right] , \end{aligned} \tag{4.51}$$

where $V_p = V(r_p)$ and

$$\psi_{a,R}(t) = \psi(t, r^*_{a,R}) , \qquad \psi_{a+1,L}(t) = \psi(t, r^*_{a+1,L}) , \tag{4.52}$$

$$\phi_{a,R}(t) = \phi(t, r^*_{a,R}) , \qquad \phi_{a+1,L}(t) = \phi(t, r^*_{a+1,L}) , \tag{4.53}$$

$$\varphi_{a,R}(t) = \varphi(t, r^*_{a,R}) , \qquad \varphi_{a+1,L}(t) = \varphi(t, r^*_{a+1,L}) , \tag{4.54}$$

and where $\tau^{a,R}_{\psi,\phi,\varphi}$ and $\tau^{a+1,L}_{\psi,\phi,\varphi}$ are (constant) penalty parameters. The structure of the penalty terms in equations (4.46)-(4.51) obeys the following rationale: The main idea behind of the penalty terms is to drive the dynamical system to satisfy a set of conditions that are not part of the original evolution equations (like constraints on the variables that have to be satisfied for all times or boundary conditions), and the strength of the driving (penalty) terms is controlled

by the penalty parameters $\tau^{a,R}_{\psi,\phi,\varphi}$ and $\tau^{a+1,L}_{\psi,\phi,\varphi}$. In our case, in Sec. 4.2, we mentioned the fact that the junction conditions (4.32) have to be imposed on the characteristic field of our system of PDEs, and these characteristic fields and their associated characteristic surfaces where given there. Therefore, we have constructed the penalty terms so that the junction conditions that are satisfied are those corresponding to the characteristic fields, that is:

$$[\,\psi^m_\ell\,]_p = 0\,, \quad [\,\phi^m_\ell \pm \varphi^m_\ell\,]_p = \pm\,\frac{S^m_\ell}{f(r_p)}\,. \tag{4.55}$$

On the other hand, ψ can be seen as a *subsidiary* variable, in the sense that we can first evolve the equations for ϕ and φ and then, use the result to evolve ψ. Then, we can use a different way of imposing the continuity of ψ, instead of the penalty method we can just replace the right-hand sides of equations (4.46) and (4.49) by

$$\partial_t\psi_{a,R} = (\phi_{a,R} + \phi_{a+1,L})/2\,, \tag{4.56}$$
$$\partial_t\psi_{a+1,L} = (\phi_{a,R} + \phi_{a+1,L})/2\,, \tag{4.57}$$

which ensures the continuity of ψ by construction and we have seen in our numerical experiments that it is numerically stable (see Sec. 5).
Regarding the global boundary conditions (*near* the horizon, $r^* = r^*_{\rm H}$, and *near* spatial infinity, $r^* = r^*_{\rm I}$), we impose them directly at the corresponding nodes, without using the penalty method (which is another option). Since we have made a first-order reduction of our original PDE (4.12), we have to adapt the outgoing/absorbing boundary conditions to the set of variables $\boldsymbol{U} = (\psi, \phi, \varphi)$. Then, the boundary conditions at $r^* = r^*_{\rm H}$ are

$$\partial_t\psi_{1,L} = \phi_{1,L}\,, \tag{4.58}$$
$$\partial_t\phi_{1,L} = -\partial_t\varphi_{1,L}\,, \tag{4.59}$$
$$\partial_t\varphi_{1,L} = \partial_{r^*}\phi_{1,L}\,, \tag{4.60}$$

and the boundary conditions at $r^* = r^*_{\rm I}$ are

$$\partial_t\psi_{D,R} = \phi_{D,R}\,, \tag{4.61}$$
$$\partial_t\phi_{D,R} = \partial_t\varphi_{D,R}\,, \tag{4.62}$$
$$\partial_t\varphi_{D,R} = \partial_{r^*}\phi_{D,R}\,, \tag{4.63}$$

and we remark that the first subdomain is number 1 and the last one is number D, the total number of subdomains.

Chapter 5

Description of the Simulations and Results

In this section we describe the results from a series of numerical experiments that show the potential of the methods just proposed. To that end, we have developed a numerical code that implements the techniques previously described. This code is based on the C language and the use of the GNU Scientific Library [Galassi et al. (2006)], mainly for calculations with special functions, and the FFTW library [Frigo & Johnson (2005)] for performing FFTs. In the implementation of the physical domain in the numerical code we have adopted a comoving tortoise coordinate: $r_c^* = r^* - r_p^*$. In this way, the particle location (and we emphasize again that we only deal with circular orbits) is always $r_c^* = 0$.

The first test we have performed is to study the evolution of a simple wave equation using the formulation and methods described in the previous sections. This case corresponds to: $\ell = m = 0$, $M = 0$ (which implies $V_\ell = 0$), and $q = 0$ (that is, no source, $\mathcal{S}_\ell^m = 0$). The test consists in following the propagation of an initial Gaussian packet in a multidomain grid and to study the convergence of the numerical scheme as the number of collocation points per subdomain, N, increases. In Figure 5.1, we show a convergence plot for a simulation that uses two subdomains, $r^* - r_p^* \in [-550\,M, 0] \cup [0, 550\,M]$, connected by the penalty method as described in subsection 4.4. The truncation error has been computed in the subdomain where the Gaussian packet is present at a chosen time. As one can see, the truncation error, estimated as the absolute value of the last spectral coefficient, $|a_N|$, decreases exponentially with the number of collocation points, as expected in the PSC method for smooth solutions. The same convergence follows for an initial Gaussian wave packet propagating on a Schwarzschild background, that is for the case in which only $\mathcal{S}_\ell^m = 0$. This is expect as the mathematical structure of the equation is essentially the same. The additional ingredient is the excitation of quasinormal modes of the black hole by the initial wave packet.

When we introduce the SCO, i.e. the particle, the situation is conceptually different. If we think in global terms, the presence of the particle implies that the global solution (the solution in the whole computational domain) will not be smooth. Hence, we cannot expect exponential convergence for the solution of our problem. However, as we have argued above, our multidomain framework avoids the presence of Dirac delta distributions in the equations by locating the particle in the interface between subdomains. Then, the presence of the particle enters through boundary conditions, actually matching conditions between subdomains. Therefore, at each domain we will have a smooth solution, and hence we expect our numerical solution to converge exponentially towards it. In our numerical experiments with a particle (remember

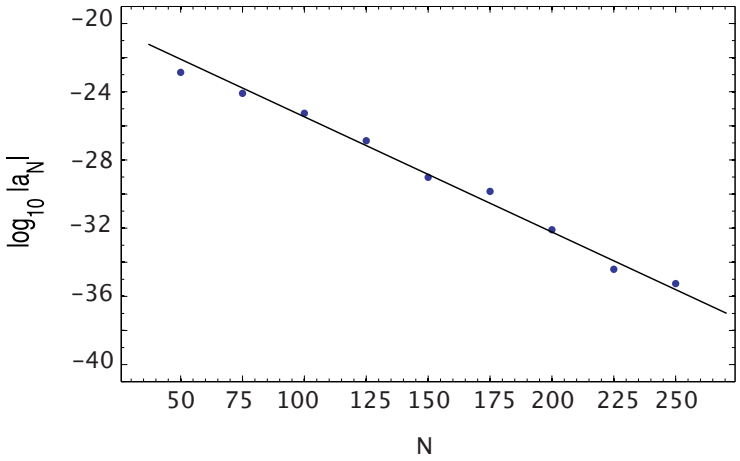

Figure 5.1: This figure shows the dependence of the truncation error (estimated by the logarithm of the absolute value of the last spectral coefficient, $\log_{10}|a_N|$, associated with the field ψ) with respect to the number of collocation points. This error corresponds to an snapshot of the evolution of the classical wave equation, for an initial condition given by a moving Gaussian packet. The data indicates the exponential convergence of the numerical method.

we restrict ourselves to the case of circular orbits), we take *zero initial data*, that is

$$\psi_\ell^m(t_o, r^*) = \phi_\ell^m(t_o, r^*) = \varphi_\ell^m(t_o, r^*) = 0\,. \tag{5.1}$$

This initial data is obviously not consistent with Einstein's equations, and as a consequence the evolution produces an initial unphysical burst. We have to wait until this unphysical features propagates away in order to analyze the solution to obtain the physically relevant results. In Figure 5.2 we show snapshots of the evolution of a scalar charged particle in circular motion at the Last Stable Orbit (LSO), in principle the most demanding case (in Schwarzschild the LSO is located at $r_p = 6\,M$). The figure includes details of the different variables, $(\psi_\ell^m, \phi_\ell^m, \varphi_\ell^m)$ for $\ell = m = 2$, near the particle location. These snapshots illustrate the ability of our method to capture the structure of the solution near the particle, in particular the ability of resolving the jump in the radial derivative of the field (snapshot on the right in Figure 5.2). In order to further validate our numerical code, we have performed simulations with the particle at the LSO changing the number of collocation points, while leaving the number of subdomains fixed. In this way we have checked that our method can achieve the exponential convergence in each individual subdomain. In Figure 5.3 we show a convergence plot obtained from simulations that use four subdomains: $r^* - r_p^* \in [-550\,M, -20\,M] \cup [-20\,M, 0] \cup [0, 20\,M] \cup [20\,M, 550\,M]$. The number of collocation points, N, is the same at each subdomain, and in this way we have more resolution near the particle, where it is most needed. The figure shows that indeed our numerical scheme has exponential convergence. The multidomain feature of our method is useful for another important reason, namely computational cost. It is not the same having N points in D domains that having $N \cdot D$ points in one single domain. This is an important point when the need for resolution comes only from some isolated regions of the computational domain, and can have dramatic consequences in the calculations. First of all, for computations in a given time step, the first option involves less calculations. Second, from the evolution point of view, in the PSC method, the Courant-Friedrichs-Lax (CFL) condition on the allowed size of the time step, Δt, is more stringent than other numerical methods as Finite Differences (FD) schemes. For the PSC method the maximum allowed time step is

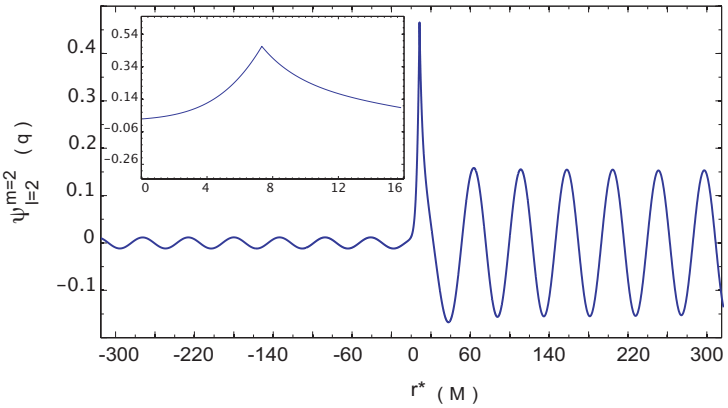

(a) Evolution of the variable ψ_ℓ^m

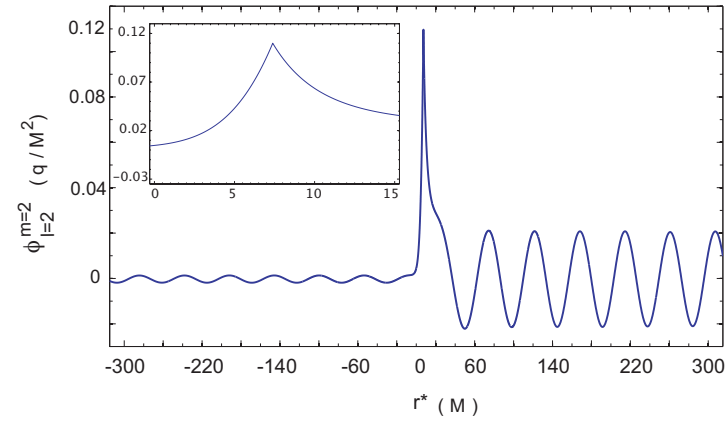

(b) Evolution of the variable ϕ_ℓ^m

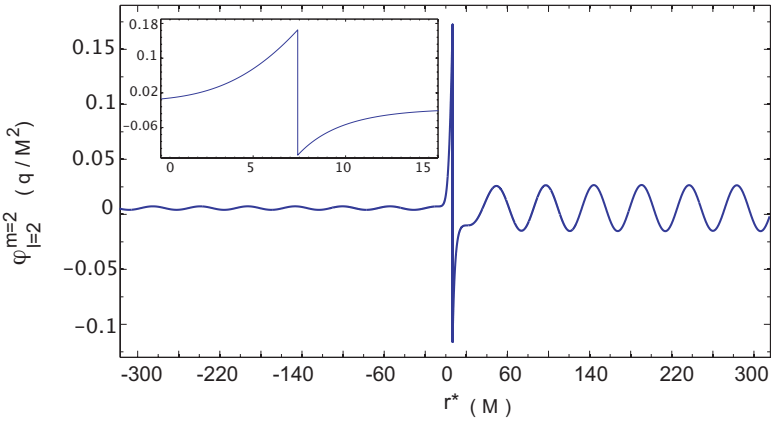

(c) Evolution of the variable φ_ℓ^m

Figure 5.2: We show snapshots of the evolution of the scalar charged particle in circular motion at the LSO for the mode $\ell = m = 2$. These simulations used 12 subdomains and 50 collocation points per subdomain. They show the evolution of the variables ψ_ℓ^m 5.2(a), ϕ_ℓ^m 5.2(b), and φ_ℓ^m 5.2(c), after a substantial time has passed and a number of wave cycles have been generated. In particular they show how the jump in the radial derivative of the field Φ_ℓ^m is resolved (this information is encoded in the variable φ_ℓ^m) in this multidomain computational framework.

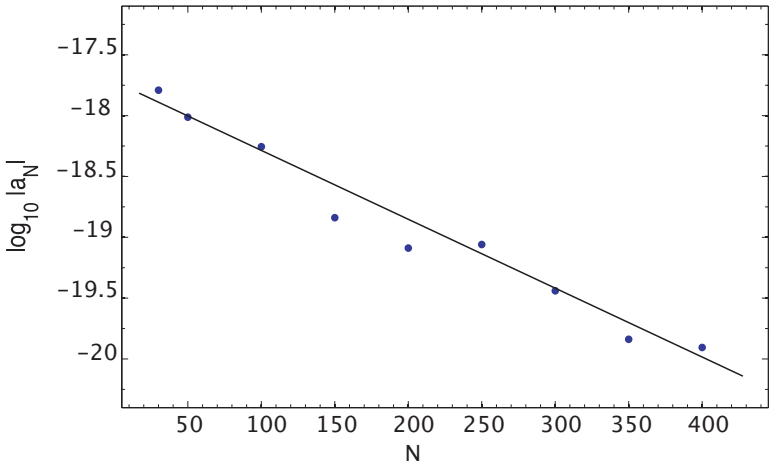

Figure 5.3: This figure shows the dependence of the truncation error ($\log_{10}|a_N|$) with respect to the number of collocation points for simulations of circular motion at the LSO ($r_p = 6\,M$) corresponding to the $\ell = m = 2$ mode, in particular for the field ψ_2^2. The data, taken from the subdomain $r^* - r_p^* \in [0, 20\,M]$ indicates the exponential convergence of the numerical method.

$\Delta t_{CFL} \sim \pi^2 |r_R^* - r_L^*|/(4N^2)$ (this is set by the minimum distance between two collocation points, which occurs at the boundaries of the subdomains, [Boyd (2001)]), that is, it goes like $1/N^2$ with respect to the number of collocation points, whereas in FD schemes it goes like $1/N$. Then, dividing the domain in subdomains can help in having a bigger Δt_{CFL}. In addition, the multidomain scheme can be seen as a way of adaptivity, in the sense that we can construct small subdomains for the regions that need to be well resolved, essentially near the particle, and large subdomains for the regions that do not need to have high resolution, essentially far away from the particle.

In order to illustrate how the multidomain feature of our numerical framework works, we have performed simulations with a fixed number of collocation points but changing the number of subdomains. The aim is to show how the solution improves by adding new subdomains. In our simulations, the most demanding region for resolution is clearly near the particle. Apart from this we have the waves leaving the particle location and going both towards the horizon and towards spatial infinity. These waves are in principle easy to resolve, but for modes with high ℓ and m we have that the source term oscillates like $\exp\{im\,\Omega_p(t - t_o)\}$ (where $\Omega_p = \sqrt{M/r_p^3}$ is the coordinate angular velocity of the particle), and hence the wavelength gets reduced so that we have many more waves that for low m. These waves are moving away and need to be resolved. In Figure 4.1 we show snapshots of evolutions with 50 collocation points per subdomain, but with different number of subdomains, namely from 2 to 16 subdomains (half of them to the left of particle and the other half to the right). The figure show the mode $\ell = 10$ and $m = 6$ (so that the period of the waves is $\pi/(3\Omega_p)$) for the three fields (ψ, ϕ, φ). We can see how for few subdomains the waves are unresolved, and that as we increase the number of subdomains the solution converges. Therefore, the multidomain structure is a very useful tool to achieve accurate results with a reasonable computational cost. The key point is to realize what is the optimal number of subdomains, their size, and their distribution over the whole computational domain. Given that in our case the period of the waves changes with the harmonic number m, the optimal strategy for setting the subdomain will depend on it. However, since the main aim of this work is to show the principal ingredients of the method and to illustrate its performance, we have not explored the possibility of changing the subdo-

main structure as m changes. However, this is something that should be done for optimizing the computational cost in the case of systematic calculations of the self-force. In this sense, it would be convenient to have a deep understanding of the computational parameter space in order to adapt these parameters to the physical ones to optimize the calculations. The next step in the validation of the code is to compute the components of the self-force acting on the charged scalar particle moving in circular geodesics around a nonrotating black hole. This is the goal of this numerical scheme, that is, to provide accurate computations of the self-force with reasonable computational cost. The calculation of the self-force require to compute the evolution of the real and imaginary parts [note that the source term in the evolution equation (4.12) is complex and hence both the real and imaginary parts are needed] of the (ℓ, m) harmonic components of Φ^m_ℓ. Since Φ is a real scalar we have that for each (ℓ, m) the relation $\bar{\Phi}^{-m}_\ell = (-1)^m \Phi^m_\ell$ holds and hence we do not need to compute the modes with $m < 0$. Given that we need to truncate the sum over (ℓ, m) at a given $\ell_{\rm max}$, the total number of evolutions that we need to run for a single self-force calculation is $N_{\rm evolutions} = [(\ell_{\rm max} + 1)(\ell_{\rm max} + 2)/2]$, where here the brackets denote the the nearest integer to the argument. For the particular case $\ell_{\rm max} = 20$, a typical case in our calculations, we need to perform $N_{\rm evolutions} = 231$ evolutions.

In Table 5.1 we present the results of the computations of the self-force vector (actually of the gradient of the regular scalar field) acting on a scalar particle in circular (geodesic) motion around a black hole at the following radii: $r/M = 6$, 7, 8, 10, 14, and 20. For these simulations we have used our multidomain framework with subdomains that contain 50 collocation points. We have used the same number of subdomains to the right and to the left of the particle. The size of these subdomains is typically $\Delta r^* = 20$, specially those near the particle. As we get far away enough from the particle towards the boundaries (typically at $r^* = \pm(500 - 700)M$), the size of the subdomains is increased since we need less resolution in those regions. The total number of subdomains that we have used ranges from $12 - 34$. We have observed that at some point increasing the number of subdomains (maintaining the size of $r^* = 20M$) does not change significantly the results. Another important point to mention is the fact that we are computing the self-force right at the particle location. But since the particle is at the interface between two subdomains, we obtain two values of the self-force components, one from the subdomain to the left [let us call it Ω_a as in equation (4.45)], $\Phi^{{\rm R},-}_\alpha = \Phi^{\rm R}_\alpha(r^*_{a,R})$, and the other one from the subdomain to the right (Ω_{a+1}), $\Phi^{{\rm R},+}_\alpha = \Phi^{\rm R}_\alpha(r^*_{a+1,L})$. This also provides us with a test of the numerical calculations as both values have to agree to a good degree of precision. In Table 5.1 we show our results and compare them with two types of calculations in the literature: (i) Calculations based on a time-domain method that uses a characteristic formulation of the scalar field equations Haas & Poisson (2006); (ii) calculations based on a frequency-domain method Diaz-Rivera et al. (2004). As we can see, we can get a good numerical approximation to the self-force components using a modest amount of computational resources. It is important to mention that these computations have a relatively low computational cost (relative to the computational cost of time-domain simulations of this sort). The average time for a full self-force calculation of the type just described in a computer with two Quad-Core Intel Xeon processors at 2.8 GHz is always in the range $20 - 30$ minutes.

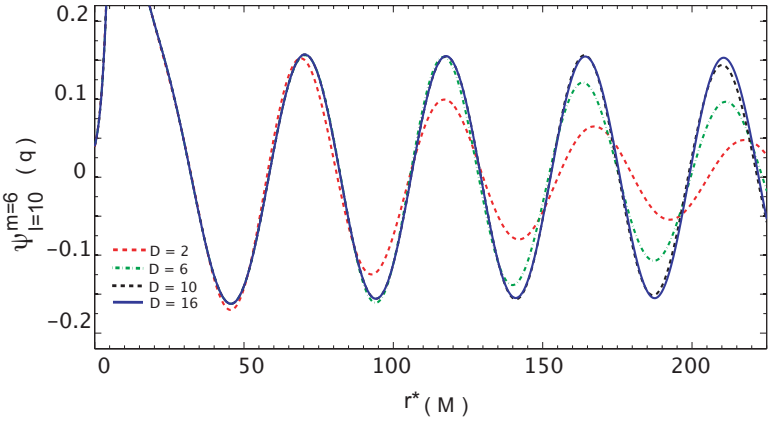

(a) Evolution of the variable ψ

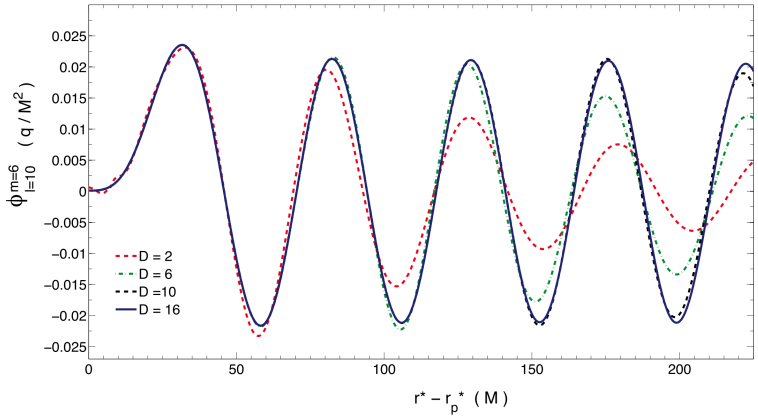

(b) Evolution of the variable ϕ

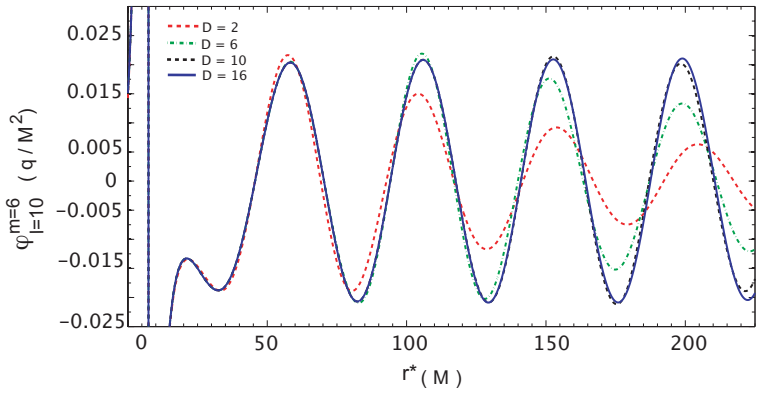

(c) Evolution of the variable φ

Figure 5.4: We show here three plots of an snapshot of the evolution of the scalar charged particle in circular orbital motion at the LSO for the mode $\ell = 10$ and $m = 6$. Each plot shows different evolutions of the variables ψ 5.4(a), ϕ 5.4(b), and φ 5.4(c), for a fixed number of collocation points ($N = 50$), but for different numbers of subdomains ($D = 2, 6, 10, 16$). In this we can see how increasing the number of subdomains leads to a better accuracy (we can see how the waves get better resolved and the solution converges as we increase the number of subdomains) with a much less computational cost as if we would have increase the number of collocation points in a single domain computational framework

Table 5.1: In this table we show the values of the regular field at the particle location, $(\Phi_\alpha^{\mathrm{R},-}, \Phi_\alpha^{\mathrm{R},+})$[1], computed at $\varphi_p = 0$. These results are obtained for for $\ell_{\max} = 20$, $N = 50$, and $D = 12 - 36$. The minimum size of the subdomains, as measured in terms of the tortoise coordinate is $\Delta r^* = 20M$, which corresponds to the subdomains near the particle location. The table shows our numerical results for different circular orbits ($r/M = 6$, 7, 8, 10, 14, and 20) and the relative errors with respect to the results obtained with a time-domain method in Haas (2007), and with a frequency-domain method in Diaz-Rivera et al. (2004) and Haas & Poisson (2006).

$r(M)$	Component of Φ_α^{R}	Estimation using the PSC Method	Estimation from Frequency-domain (a,b)	Error relative to Frequency-domain (a,b)	Error relative to Time-domain (c)
6	$(\Phi_t^{\mathrm{R},-}, \Phi_t^{\mathrm{R},+})$	$(3.60777, 3.60778) \cdot 10^{-4}$	$3.609072 \cdot 10^{-4}$	$(0.03, 0.03)\%$	$(0.12, 0.12)\%$
	$(\Phi_r^{\mathrm{R},-}, \Phi_r^{\mathrm{R},+})$	$(1.67364, 1.67362) \cdot 10^{-4}$	$1.67728 \cdot 10^{-4}$	$(0.2, 0.2)\%$	$(0.18, 0.18)$ %
	$(\Phi_\varphi^{\mathrm{R},-}, \Phi_\varphi^{\mathrm{R},+})$	$(-5.3042, -5.3044) \cdot 10^{-3}$	$-5.304231 \cdot 10^{-3}$	$(4 \cdot 10^{-4}, 10^{-3})$ %	$(6 \cdot 10^{-4}, 10^{-3})\%$
7	$(\Phi_t^{\mathrm{R},-}, \Phi_t^{\mathrm{R},+})$	$(1.76638, 1.76639) \cdot 10^{-4}$			
	$(\Phi_r^{\mathrm{R},-}, \Phi_r^{\mathrm{R},+})$	$(7.84007, 7.84001) \cdot 10^{-5}$	$7.85067 \cdot 10^{-5}$	$(0.13, 0.13)$ %	
	$(\Phi_\varphi^{\mathrm{R},-}, \Phi_\varphi^{\mathrm{R},+})$	$(-3.2730, -3.2733) \cdot 10^{-3}$			
8	$(\Phi_t^{\mathrm{R},-}, \Phi_t^{\mathrm{R},+})$	$(9.76454, 9.76457) \cdot 10^{-5}$			
	$(\Phi_r^{\mathrm{R},-}, \Phi_r^{\mathrm{R},+})$	$(4.0835, 4.0832) \cdot 10^{-5}$	$4.08250 \cdot 10^{-5}$	$(0.02, 0.01)$ %	
	$(\Phi_\varphi^{\mathrm{R},-}, \Phi_\varphi^{\mathrm{R},+})$	$(-2.2115, -2.2108) \cdot 10^{-3}$			
10	$(\Phi_t^{\mathrm{R},-}, \Phi_t^{\mathrm{R},+})$	$(3.74362, 3.74363) \cdot 10^{-5}$			
	$(\Phi_r^{\mathrm{R},-}, \Phi_r^{\mathrm{R},+})$	$(1.3804, 1.3801) \cdot 10^{-5}$	$1.37844 \cdot 10^{-5}$	$(0.14, 0.12)$ %	
	$(\Phi_\varphi^{\mathrm{R},-}, \Phi_\varphi^{\mathrm{R},+})$	$(-1.1860, -1.1858) \cdot 10^{-3}$			
14	$(\Phi_t^{\mathrm{R},-}, \Phi_t^{\mathrm{R},+})$	$(9.17691, 9.17691) \cdot 10^{-6}$			
	$(\Phi_r^{\mathrm{R},-}, \Phi_r^{\mathrm{R},+})$	$(2.7269, 2.7266) \cdot 10^{-6}$	$2.72008 \cdot 10^{-6}$	$(0.25, 0.24)$ %	
	$(\Phi_\varphi^{\mathrm{R},-}, \Phi_\varphi^{\mathrm{R},+})$	$(-4.8383, -4.8389) \cdot 10^{-4}$			
20	$(\Phi_t^{\mathrm{R},-}, \Phi_t^{\mathrm{R},+})$	$(2.08859, 2.08858) \cdot 10^{-6}$			
	$(\Phi_r^{\mathrm{R},-}, \Phi_r^{\mathrm{R},+})$	$(4.9444, 4.9440) \cdot 10^{-7}$	$4.93790 \cdot 10^{-7}$	$(0.13, 0.12)$ %	
	$(\Phi_\varphi^{\mathrm{R},-}, \Phi_\varphi^{\mathrm{R},+})$	$(-1.9245, -1.9244) \cdot 10^{-4}$			

1. We show the values of the gradient of the regular field instead of the components of the self-force for the sake of comparing with other results in the literature.

(a) calculations in Diaz-Rivera et al. (2004).

(b) calculations in Haas & Poisson (2006).

(c) calculations in Haas (2007).

Chapter 6

Conclusions and Discussion

In this dissertation we have introduced a new time-domain technique for the simulations of EMRIs. The main ingredient of the method is to use a multi-domain framework in which the SCO, described as a point-like object, is located at the interface between two subdomains. In this way we have shown that this technique enjoys the exponential convergence property of the PSC method and its accuracy and, at the same time, it is also an efficient method to make time-domain computations of the self-force. We have achieved a good accuracy in these computations by using a relatively low number of collocation points. In this regard, the multidomain framework allows us to locate more collocation points in the region where they are most needed, i.e. around the particle. This is done by choosing appropriately the number of subdomains, their size, and location. Another positive property of our numerical scheme is that it can be easily parallelized to be used in supercomputers, as we can assign the work of each subdomain to different CPUs. The only information that we need to communicate is the one necessary to satisfy the matching conditions between subdomains.
The calculations performed for this work show the potential of this multidomain technique for the description of EMRIs in time domain. These results still leave room for improvement as we have not explore yet the full parameter space of the numerical method (number of collocation points per subdomain, number and distribution of subdomains, parameters of the spectral filter, penalty parameters, etc), which is wide enough.
In the future we will study how to extend our computational framework in order to include eccentric orbits. The main difficulty is obviously to deal with a particle moving in the radial direction. Notice that our present framework assumes that it is located at a fixed value due that we are dealing with circular motion. There are several ways in which we can attack this problem. One is to try to implement some type of moving grid technique (as it was done in a similar situation in Sopuerta & Laguna (2006)), but the reconstruction of the grid at every time step could increase significantly the computational cost of the evolution. Another possibility is to try to make a change of coordinates to coordinates comoving with the particle, so that the techniques presented in this work can be implemented in a straightforward way.
On the other hand, we expect that MBHs sitting at galactic centers will have considerable spins ($a/M \sim 0.7$ or bigger, where a is the Kerr spin parameter) and hence the MBH should be described by the Kerr metric instead of the Schwarzschild metric. This means to have a less symmetric background, instead of the spherical symmetry of Schwarzschild just the axisymmetry of Kerr. In that case one can separate the dependence on the azimuthal angle and is left with $2+1$ wave-type equations with singular terms. The main difficulty in this case is that each m-mode (coming from the separation of the azimuthal angle) diverges logarithmically at the particle location. Then, before trying to transfer the techniques presented in this work to

the Kerr case, one has to apply before a regularization procedure as it has been done in [Barack & Golbourn (2007); Vega & Detweiler (2008); Lousto & Nakano (2008)]. Apart from this, we expect that most of the methods presented in this work will be helpful in achieving efficient simulations of EMRIs in the case of a spinning MBH.

This dissertation is based in recent work presented in Canizares & Sopuerta (2008) and Canizares & Sopuerta (2009).

Appendix A

Conventions in this work for Special Funcions

Here, we summarize the main conventions used for the special functions involved in calculations of this work.

A.1 Spherical Harmonics

The expression we use for the scalar spherical harmonics is:

$$Y_\ell^m(\theta,\varphi) = \sqrt{\frac{2\ell+1}{4\pi}\frac{(\ell-m)!}{(\ell+m)!}}\, P_\ell^m(\cos\theta) e^{im\varphi}\,, \tag{A.1}$$

where P_ℓ^m are the associated Legendre polynomials [we use the same expressions as in [Abramowitz & Stegun (1972)], equations (8.6.6) and (8.6.18)]

$$P_\ell^m(x) = \frac{(-1)^{\ell+m}}{2^\ell\,\ell!}(1-x^2)^{m/2}\frac{d^{\ell+m}}{dx^{\ell+m}}(1-x^2)^\ell\,, \tag{A.2}$$

where ℓ is a non-negative integer and m is an integer restricted to the following range: $m \in (-\ell\,, -\ell+1\,, \ldots\,, \ell-1\,, \ell)$.
Through this work we have used the identities

$$P_\ell^{-m} = (-1)^m \frac{(\ell-m)!}{(\ell+m)!} P_\ell^m \tag{A.3}$$

$$\bar{Y}_\ell^m(\theta,\varphi) = (-1)^m Y_\ell^{-m}(\theta,\varphi). \tag{A.4}$$

A.2 Hypergeometric Functions

The classical standard hypergeometric series is given by:

$${}_2F_1(a,b;c;z) = \sum_{n=0}^{\infty} \frac{(a)_n (b)_n}{(c)_n}\,\frac{z^n}{n!} \tag{A.5}$$

where $(a)n = a(a+1)(a+2)(a+n-1)$ is the rising factorial. Hypergeometric functions are solutions to hypergeometric differential equations, which is a general second-order ordinary differential equation.
Rewriting the series as

$$ {}_2F_1(a,b;c;z) = 1 + \sum_{n=1}^{\infty} \alpha_n z^n, \tag{A.6}$$

where $\alpha_n = \frac{(a)_n (b)_n}{(c)_n n!}$, one obtains that:

- if either a or b is a negative integer, the series only has a finite number of terms
- if c is a negative integer, the series is not well-defined because all the denominators are zero after a certain point
- as $n \to \infty$, the ratio of successive coefficients a_{n-1}/a_n approaches one in the limit
- the series is in general a convergent power series for values of z such that $|z| < 1$

It can also be shown [Abramowitz & Stegun (1972)] that if c is not a negative integer, the series converges when $z = 1$ if $\Re(c-a-b) > 0$. In this important case the value ${}_2F_1(a,b;c;1)$ is given by

$$ {}_2F_1(a,b;c;1) = \frac{\Gamma(c)\Gamma(c-a-b)}{\Gamma(c-a)\Gamma(c-b)} \tag{A.7}$$

where $\Gamma(x)$ denotes the gamma function.
The coefficients F_Q can be computed in terms of hypergeometric functions as follows (see [Abramowitz & Stegun (1972)]):

$$ F_Q = {}_2F_1\left(Q, \frac{1}{2}; 1; \frac{M}{r_p f(r_p)}\right) . \tag{A.8}$$

Bibliography

Abramowitz, M. & Stegun, I. A., 1972. *Handbook of Mathematical Functions with Formulas, Graphs, and Mathematical Tables*. Dover, New York.

Baker, J. G., Centrella, J., Choi, D.-I., Koppitz, M. & van Meter, J., 2006. Gravitational wave extraction from an inspiraling configuration of merging black holes. *Phys. Rev. Lett.*, **96**, 111102.

Barack, L., 2000. Self-force on a scalar particle in spherically-symmetric spacetime via mode-sum regularization: Radial trajectories. *Phys. Rev.*, **D62**, 084027.

Barack, L., 2001. Gravitational self-force by mode sum regularization. *Phys. Rev.*, **D64**, 084021.

Barack, L. & Golbourn, D. A., 2007. Scalar-field perturbations from a particle orbiting a black hole using numerical evolution in 2+1 dimensions. *Phys. Rev.*, **D76**, 044020.

Barack, L., Mino, Y., Nakano, H., Ori, A. & Sasaki, M., 2002. Calculating the gravitational self force in Schwarzschild spacetime. *Phys. Rev. Lett.*, **88**, 091101.

Barack, L. & Ori, A., 2000. Mode sum regularization approach for the self force in black hole spacetime. *Phys. Rev.*, **D61**, 061502.

Barack, L. & Ori, A., 2002. Regularization parameters for the self force in Schwarzschild spacetime. I: Scalar case. *Phys. Rev.*, **D66**, 084022.

Barack, L. & Ori, A., 2003. Regularization parameters for the self force in Schwarzschild spacetime: II. gravitational and electromagnetic cases. *Phys. Rev.*, **D67**, 024029.

Barut, A. O., 1980. *Electrodynamics and Classical Theory of Fields and Particles*. Dover, New York.

Boyd, J. P., 2001. *Chebyshev and Fourier Spectral Methods*. Dover, New York, 2nd ed.

Brandt, S. & Bruegmann, B., 1997. Black hole punctures as initial data for general relativity. *Phys. Rev. Lett.*, **78**, 3606–3609.

Brown, D. A. et al., 2007. Gravitational waves from intermediate-mass-ratio inspirals for ground-based detectors. *Phys. Rev. Lett.*, **99**, 201102.

Butcher, J. C., 2008. *Numerical Methods for Ordinary Differential Equations*. John Wiley and Sons, Chichester, 2nd ed.

Campanelli, M., Lousto, C. O., Marronetti, P. & Zlochower, Y., 2006. Accurate Evolutions of Orbiting Black-Hole Binaries Without Excision. *Phys. Rev. Lett.*, **96**, 111101.

Canizares, P. & Sopuerta, C. F., 2008. Simulations of Extreme-Mass-Ratio Inspirals Using Pseudospectral Methods. In *Proceedings of the 7th International LISA Symposium*.

Canizares, P. & Sopuerta, C. F., 2009. An Efficient Pseudospectral Method for the Computation of the Self-force on a Charged Particle: Circular Geodesics around a Schwarzschild Black Hole.

Cutler, C., Kennefick, D. & Poisson, E., 1994. Gravitational radiation reaction for bound motion around a Schwarzschild black hole. *Phys. Rev.*, **D50**, 3816–3835.

Davis, M., Ruffini, R. & Tiomno, J., 1972. Pulses of Gravitational Radiation of a Particle Falling Radially into a Schwarzschild Black Hole. *PRD*, **5**, 2932–2935.

Detweiler, S., Messaritaki, E. & Whiting, B. F., 2003. Self-force of a scalar field for circular orbits about a Schwarzschild black hole. *Phys. Rev.*, **D67**, 104016.

Detweiler, S. & Whiting, B. F., 2003. Self-force via a Green's function decomposition. *Phys. Rev.*, **D67**, 024025.

Detweiler, S. L., 1978. Black holes and gravitational waves. I - Circular orbits about a rotating hole. *ApJ*, **225**, 687–693.

Detweiler, S. L. & Szedenits, Jr., E., 1979. Black holes and gravitational waves. II - Trajectories plunging into a nonrotating hole. *ApJ*, **231**, 211–218.

Diaz-Rivera, L. M., Messaritaki, E., Whiting, B. F. & Detweiler, S., 2004. Scalar field self-force effects on orbits about a Schwarzschild black hole. *Phys. Rev.*, **D70**, 124018.

Finn, L. S. & Thorne, K. S., 2000. Gravitational waves from a compact star in a circular, inspiral orbit, in the equatorial plane of a massive, spinning black hole, as observed by LISA. *Phys. Rev.*, **D62**, 124021.

Frigo, M. & Johnson, S. G., 2005. The Design and Implementation of FFTW3. *Proceedings of the IEEE*, **93**(2), 216–231. Special issue on "Program Generation, Optimization, and Platform Adaptation".

Gair, J. R., Barack, L., Creighton, T., Cutler, C., Larson, S. L., Phinney, E. S. & Vallisneri, M., 2004. Event rate estimates for LISA extreme mass ratio capture sources. *Class. Quant. Grav.*, **21**, S1595–S1606.

Galassi, M., Davies, J., Theiler, J., Gough, B., Jungman, G., Booth, M. & Rossi, F., 2006. *GNU Scientific Library Reference Manual*. Network Theory Ltd., Bristol, 2nd ed.

Grandclement & Novak, 2009. Spectral Methods for Numerical Relativity. *Living Reviews in Relativity*, **12**(1). URL `http://www.livingreviews.org/lrr-2009-1`.

Haas, R., 2007. Scalar self-force on eccentric geodesics in Schwarzschild spacetime: a time-domain computation. *Phys. Rev.*, **D75**, 124011.

Haas, R. & Poisson, E., 2006. Mode-sum regularization of the scalar self-force: Formulation in terms of a tetrad decomposition of the singular field. *Phys. Rev.*, **D74**, 044009.

Hesthaven, J. S., 2000. *Applied Numerical Mathematics*, **33**, 23–41.

Hinderer, T. & Flanagan, E. E., 2008. Two timescale analysis of extreme mass ratio inspirals in Kerr. I. Orbital Motion.

Hopman, C. & Alexander, T., 2006. The effect of mass-segregation on gravitational wave sources near massive black holes. *Astrophys. J.*, **645**, L133–L136.

Hulse, R. A. & Taylor, J. H., 1975. Discovery of a pulsar in a binary system. *ApJ*, **195**, L51–L53.

Jackson, J. D., 1999. *Classical Electrodynamics*. John Wiley & Sons, New York, 3rd ed.

Lousto, C. O. & Nakano, H., 2008. A new method to integrate (2+1)-wave equations with Dirac's delta functions as sources. *Class. Quant. Grav.*, **25**, 145018.

Mandel, I., Brown, D. A., Gair, J. R. & Miller, M. C., 2007. Rates and Characteristics of Intermediate-Mass-Ratio Inspirals Detectable by Advanced LIGO.

Mino, Y., 2003. Perturbative Approach to an orbital evolution around a Supermassive black hole. *Phys. Rev.*, **D67**, 084027.

Mino, Y., 2008. Modulation of the gravitational waveform by the effect of radiation reaction. *Phys. Rev.*, **D77**, 044008.

Mino, Y., Nakano, H. & Sasaki, M., 2003. Covariant self-force regularization of a particle orbiting a Schwarzschild black hole: Mode decomposition regularization. *Prog. Theor. Phys.*, **108**, 1039–1064.

Mino, Y., Sasaki, M. & Tanaka, T., 1997. Gravitational radiation reaction to a particle motion. *Phys. Rev.*, **D55**, 3457–3476.

Poisson, E., 1995. Gravitational radiation from a particle in circular orbit around a black hole. 6. Accuracy of the postNewtonian expansion. *Phys. Rev.*, **D52**, 5719–5723.

Poisson, E., 1997. Erratum and Addendum: Gravitational radiation from a particle in circular orbit around a black hole. VI. Accuracy of the post-Newtonian expansion. *Phys. Rev.*, **D55**, 7980–7981.

Poisson, E., 2004. The motion of point particles in curved spacetime. *Living Rev. Relativity*, **7**, 6. URL `http://www.livingreviews.org/lrr-2004-6`.

Poisson, E., 2005. The Gravitational Self-force. In P. Florides, B. Nolan & A. Ottewill, eds., *General Relativity and Gravitation*, 119–+.

Pound, A. & Poisson, E., 2008. Multi-scale analysis of the electromagnetic self-force in a weak gravitational field. *Phys. Rev.*, **D77**, 044012.

Pound, A., Poisson, E. & Nickel, B. G., 2005. Limitations of the adiabatic approximation to the gravitational self-force. *Phys. Rev.*, **D72**, 124001.

Press, W. H., Flannery, B. P., Teukolsky, S. A. & Vetterling, W. T., 1992. *Numerical Recipes: The Art of Scientific Computing*. Cambridge University Press, Cambridge.

Quinn, T. C., 2000. Axiomatic approach to radiation reaction of scalar point particles in curved spacetime. *Phys. Rev.*, **D62**, 064029.

Quinn, T. C. & Wald, R. M., 1997. An axiomatic approach to electromagnetic and gravitational radiation reaction of particles in curved spacetime. *Phys. Rev.*, **D56**, 3381–3394.

Regge, T. & Wheeler, J. A., 1957. Stability of a Schwarzschild Singularity. *Phys. Rev.*, **108**, 1063–1069.

Sigurdsson, S. & Rees, M. J., 1996. Capture of stellar–mass compact objects by massive black holes in galactic cusps.

Sopuerta, C. F. & Laguna, P., 2006. Finite element computation of the gravitational radiation emitted by a point-like object orbiting a non-rotating black hole. *Phys. Rev.*, **D73**, 044028.

Sopuerta, C. F., Sun, P., Laguna, P. & Xu, J., 2005. A toy model for testing finite element methods to simulate extreme-mass-ratio binary systems.

Thorne, K. S., 1997. Probing black holes and relativistic stars with gravitational waves.

Vega, I. & Detweiler, S., 2008. Regularization of fields for self-force problems in curved spacetime: foundations and a time-domain application. *Phys. Rev.*, **D77**, 084008.

Wald, R., 1984. *General Relativity*. The University of Chicago press, Chicago.

Weinberg, S., 1972. *Gravitation and Cosmology. Principles and Applications of The General Theory of Relativity*. John Wiley & Sons, New York.

Weisberg, J. M. & Taylor, J. H., 2005. The Relativistic Binary Pulsar B1913+16: Thirty Years of Observations and Analysis. In F. A. Rasio & I. H. Stairs, eds., *Binary Radio Pulsars*, vol. 328 of *Astronomical Society of the Pacific Conference Series*, 25–+.

Zerilli, F. J., 1970. Gravitational Field of a Particle Falling in a Schwarzschild Geometry Analyzed in Tensor Harmonics. *PRD*, **2**, 2141–2160.